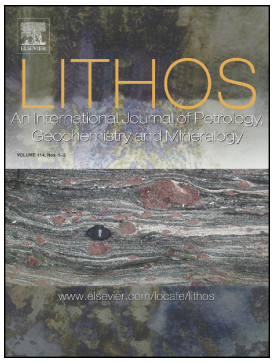

Middle-Late Jurassic magmatism in the west central Lhasa subterrane, Tibet: Petrology, zircon chronology, elemental and Sr-Nd-Pb-Hf-Mg isotopic geochemistry

Xin Tong, Jingjing Yan, Zhidan Zhao, Yaoling Niu, Ningyuan Qi, Qingshang Shi, Dong Liu, Qing Wang, Liang-Liang Zhang, Guochen Dong, Di-Cheng Zhu

PII: S0024-4937(21)00592-2

DOI: https://doi.org/10.1016/j.lithos.2021.106549

Reference: LITHOS 106549

To appear in: *LITHOS*

Received date: 30 June 2021

Revised date: 23 November 2021

Accepted date: 23 November 2021

Please cite this article as: X. Tong, J. Yan, Z. Zhao, et al., Middle-Late Jurassic magmatism in the west central Lhasa subterrane, Tibet: Petrology, zircon chronology, elemental and Sr-Nd-Pb-Hf-Mg isotopic geochemistry, *LITHOS* (2021), https://doi.org/10.1016/j.lithos.2021.106549

Middle-Late Jurassic magmatism in the west central Lhasa subterrane, Tibet: Petrology, zircon chronology, elemental and Sr-Nd-Pb-Hf-Mg isotopic geochemistry

Xin Tong[a,b], Jingjing Yan[a,c], Zhidan Zhao[a,*] zdzhao@cugb.edu.cn**, Yaoling Niu[a,d,e,f], Ningyuan Qi[a], Qingshang Shi[a], Dong Liu[a], Qing Wang[a], Liang-Liang Zhang[a], Guochen Dong[a], Di-Cheng Zhu[a]**

[a]*State Key Laboratory of Geological Processes and Mineral Resources, and School of Earth Sciences and Resources, China University of Geosciences, Beijing, 100083, China*

[b]*Tianjin Center, China Geological Survey, Tianjin, 300170, China*

[c]*Key Laboratory of Agro-Product Quality and Safety, Ministry of Agriculture and Rural Affairs, Institute of Quality Standard and Testing Technology for Agro-Products, Chinese Academy of Agricultural Sciences, 100081, Beijing, China*

[d]*Department of Earth Sciences, Durham University, Durham DH1 3LE, UK*

[e]*Laboratory for Marine Geology, Qingdao National Laboratory for Marine Science and Technology, Qingdao 266061, China*

[f]*Institute of Oceanology, Chinese Academy of Sciences, Qingdao 266071, China*

[*]Corresponding author.

Abstract

Mesozoic magmatic rocks are widespread in the Lhasa terrane, but most of them are of cretaceous age. Because Jurassic rocks are relatively rare and our knowledge on such earlier magmatism in the context of the tectonic setting and evolution is limited. In this study, we focus on the mid-late Jurassic granitoids that occur in the west central Lhasa subterrane. We present the results of a systematic study of these granitoid rocks of tonalite composition

together with the hosted mafic magmatic enclaves. We dated 4 representative tonalite samples and 2 enclaves using zircon U-Pb method that gives the age range of 167-154 Ma. All these samples have Sr-Nd-Pb isotopic compositions ($^{87}Sr/^{86}Sr$ = 0.713941-0.718417, $\varepsilon_{Nd}(t)$ = −14 to −9.8, $^{206}Pb/^{204}Pb$ = 18.806–18.936, $^{207}Pb/^{204}Pb$ = 15.739–15.764, $^{208}Pb/^{204}Pb$ = 39.257–39.798) similar to the composition of gneisses from the basement of the Lhasa terrane, suggesting that magmas parental to these mid-late Jurassic granitoids of tonalitic composition are of largely crustal origin, which is also supported by the petrographic observations. Both of the tonalite samples and the mafic enclaves have a wide span of zircon $\varepsilon_{Hf}(t)$ of −15.9 to −0.2 and −13.8 to −7.4, respectively. These samples also show varying $\delta^{26}Mg$ ranging from −0.40 to −0.18, with an average $\delta^{26}Mg$ = −0.27 ± 0.06‰ (2SD) that is best understood as representing the Mg composition of the continental crust of the Lhasa terrane. All these observations allow us to conclude that basaltic melts derived from metasomatized mantle were involved in the petrogenesis of these granitoids. Specifically, southward subduction of the Bangong-Nujiang Ocean lithosphere and subsequent slab rollback metasomatized the mantle wedge and the lithospheric mantle above, whose melting produced basaltic magmas. Underplating and intrusion of these basaltic magmas caused crustal melting and generation of granitoid magmas parental to the tonalite and enclaves we study.

Keywords

Tonalite, Sr-Nd-Pb-Mg isotope, Geochronology, Tethyan Bangong-Nujiang Ocean, Lhasa terrane.

1 Introduction

The Tibetan Plateau is a geological amalgamation of several continental collision events since the Early Paleozoic (cf. Kapp et al., 2007; Yin and Harrison, 2000; Zhu et al., 2009; 2010). The ongoing India-Asia continental convergence since the collision ca. 55 Ma has been uplifting the Greater Tibetan Plateau (including the Qiangtang, Lhasa and Tethyan Himalayan terranes) (cf. Liu et al., 2014; Zhu et al., 2013). Much has been learned in the past decades about the complexities of the deformation style and magmatism in response to the collision and the continued convergence (Chung et al., 2005; Sengör et al., 1993; Yin and Harrison, 2000; Zhu et al., 2013). However, to better understand the history of the Tibetan Plateau requires the knowledge of the nature of its pre-collisional lithosphere.

The Lhasa terrane is the southernmost Eurasian block rifted from Gondwana and drifted across the Tethyan Ocean before colliding with the Qiangtang terrane in the early Cretaceous (Zhu et al., 2011, 2013; Fan et al., 2021). The northward subduction of the Neo-Tethyan seafloor marked by the Indus-Yarlung suture zones led to the Jurassic to Cretaceous magmatism and associated Cu-Au mineralization in the southern Lhasa subterrane (Ji et al., 2009; Tafti et al., 2014; Tang et al., 2015; Wen et al., 2008a; Zhu et al., 2011; Dong et al., 2020; Gao et al., 2021). So far much of the research has focused on the Early-Late Cretaceous magmatism widespread in the central and northern Lhasa subterranes with petrotectonic models of varying sophistication (e.g., Zhu et al., 2009, 2011, 2016; Sui et al., 2013; Cao et al., 2016; DeCelles et al., 2007; Kapp et al., 2005, 2007; Pan et al., 2012), but our knowledge of the Jurassic magmatism is rather limited largely because of rare outcrops that have been recognized far to the west of the central Lhasa subterrane (Fig.1).

In this paper, we report the results of our systematic study of the Middle-Late Jurassic granitoids and their hosted enclaves from the west central Lhasa subterrane using a combined approach of electron probe microanalysis, zircon geochronology, bulk-rock elemental and Sr-Nd-Pb isotope geochemistry as well as zircon Hf isotope composition. We have also

conducted bulk-rock Mg isotope analysis to discuss possible mantle contribution to the magmatism and the average magnesium isotope composition of the crust in the central Lhasa subterrane. Our new data, together with the literature data, allow us (i) to discuss the nature and petrogenesis of the granitoids, (ii) to clarify their relationship with seafloor subduction of the Neo-Tethyan Ocean and the Bangong–Nujiang Ocean, and (iii) to better understand the deep geodynamic processes in the Middle-Late Jurassic time period beneath the central Lhasa subterrane.

2 Geological setting and sampling

The Tibetan Plateau formed as the result of the Paleotethyan ocean closure and subsequent amalgamation of Gondwana-derived micro-continental blocks and intra-oceanic arc terranes (Zhu et al., 2013). It consists primarily of three terranes, which are, from south to north, the Lhasa terrane, Qiangtang terrane and Songpan-Ganze terrane, separated by the Bangong-Nujiang and Jinsha sutures respectively (Fig.1).

The Bangong-Nujiang suture zone (Fig.1), which extends over 2000 km across the central Tibetan Plateau, is characterized by scattered Late Triassic-Early Cretaceous ophiolite fragments (cf. Li et al., 2014a; Zhu et al., 2011). The Indus-Yarlung Zangbo suture zone separates the Lhasa terrane from the Indian continent to the south and contains remnants of the Neo-Tethyan seafloor lithologies (cf. Yin and Harrison, 2000; Zhu et al., 2013). The Lhasa terrane can be further subdivided into the northern, central, and southern subterranes, separated by the Shiquan River-Nam Tso Mélange Zone and Luobadui-Milashan Fault, respectively (Fig. 1, Zhu et al., 2011).

The southern Lhasa subterrane is dominated by the Cretaceous-Tertiary Gangdese Batholith and Palaeogene Linzizong volcanic succession (Ji et al., 2009; Zhu et al., 2013).

Abundant isotope data for these magmatic rocks indicate that, the southern Lhasa subterrane is characterized by juvenile crust with limited Precambrian basement (e.g., Mo et al., 2007, 2008, 2009; Dong et al., 2010; Zhu et al., 2011, 2013). The sedimentary cover in this subterrane includes Late Triassic-Cretaceous volcano-sedimentary strata.

The central Lhasa subterrane has been interpreted as a microcontinent with a Precambrian basement, which is covered with Permo-Carboniferous metasedimentary rocks and an upper Jurassic-lower Cretaceous volcano-sedimentary sequence (Kapp et al., 2005; Volkmer et al., 2007; Zhu et al., 2011, 2013). These Mesozoic volcanic rocks are predominantly silicic lavas and volcaniclastic rocks (Zhu et al., 2011). Mesozoic plutonic rocks also occur in this subterrane as batholiths of varying size, and extend discretely along strike of the subterrane (Fig.1, Zhu et al., 2011).

The northern Lhasa subterrane is also characterized by juvenile crust with no basement rocks so far recognized (Zhu et al., 2011, 2013). The sedimentary cover in this subterrane is dominantly Jurassic-Cretaceous sedimentary rocks and Early Cretaceous volcano-sedimentary sequence (Zhu et al., 2011). Mesozoic plutons generally occur as huge batholiths in this subterrane, intruding the Jurassic-Cretaceous sequences (Fig.1, Zhu et al., 2011, 2013).

As mentioned above, the Mesozoic magmatism is widespread in the central and northern Lhasa subterranes, but the granitoids of Middle-Late Jurassic age are restricted in the west central Lhasa subterrane (Fig.1). All the samples of this study are least altered and collected from the Shiquanhe Pluton, in the west central Lhasa subterrane (Fig.1). The Shiquanhe Pluton extends from the east of Gar County to the northeast of Zuozuo with an outcrop area of ~ 600 km^2 (Fig.2). The pluton is dominated by tonalite, diorite and granodiorite with the more felsic veins in places. Abundant mafic enclaves are present in the pluton and have sharp contacts with the host (Fig.3a,b). A total of 25 host tonalite and 9 mafic enclave samples are collected in this study (Table 1).

3 Petrography

The host tonalite is grey-colored, medium- to coarse-grained with equigranular texture, consisting of amphibole (Amp, 35%-45%), plagioclase (Pl, 50%), minor quartz (Q, 10%-15%) and biotite (Bi, 2%-3%) with accessory apatite (Ap), zircon (Zr) etc. (Fig.3c,d). Amphibole and plagioclase are euhedral to subhedral, whereas quartz and biotite are subhedral to anhedral (Fig.3c,d). Some plagioclase crystals show clay alteration (Fig.3c,d).

The enclaves are mafic diorite dominated by amphibole (50%-55%) and plagioclase (40%-45%) with minor clinopyroxene (Cpx, 3%) and quartz (5%) (Fig.3e,f). Plagioclase is altered to various degree. Most of these enclaves have an equigranular texture, but coarser-grained amphibole crystals are poikilocrysts (Fig.3e,f) with mineral inclusions the same mineral assemblage as in the matrix.

4 Analytical methods

4.1 Electron probe microanalysis (EPMA) of minerals

Electron probe micro-analysis of minerals was carried out in the Institute of Geology and Geophysics, Chinese Academy of Sciences (IGGCAS), Beijing. A five-spectrometer Cameca SX-100 electron microprobe analyzer was used with an accelerating voltage of 15 kV and beam current of 10 nA. The precision of all analyzed elements was better than 1.5%.

4.2 Zircon U-Pb dating and Hf isotopes

Zircon extraction was done through a combined method of sample crushing, and heavy liquid and magnetic separation. Representative zircon grains were hand-picked and mounted

on adhesive tape, embedded in epoxy resin, polished to about half their size and photographed in reflected and transmitted light. Zircon structures were also studied using cathode luminescence (CL) imaging.

Zircon U-Pb dating was carried out in the Institute of Oceanology, Chinese Academy of Sciences, Qingdao, using a laser ablation-inductively coupled plasma mass spectrometry (LA-ICPMS). The detailed operating conditions for the laser ablation system, the ICP-MS instrument, and data reduction followed those described in Liu et al. (2010b). Zircon 91500 was used as an external standard and zircon GJ-1 was analyzed as internal standard. ICPMSDataCal (Liu et al., 2010) was used for data reduction and ISOPLOT (ver. 3.0) (Ludwig, 2003) was used for age calculation for plotting the Concordia diagrams.

Zircon in *situ* Hf isotope analysis for SQ1624 and SQ1626 was carried out in the State Key Laboratory of Geological Processes and Mineral Resources, China University of Geosciences, Wuhan, using a Neptune Plus MC-ICPMS (Thermo Fisher Scientific, Germany), coupled to a GeoLas 2005 Excimer ArF laser-ablation system with a beam size of 44 μm and laser pulse frequency of 10 Hz. For SQ1637 and SQ1640, the analysis was conducted using the same MC-ICPMS instrument, but equipped a 193 nm Excimer ArF laser-ablation system (NewWave 193^{UC}) in Milma Lab, China University of Geosciences, Beijing, with a beam size of 35 μm. Zircon 91500 was used as an external standard and zircon GJ-1 was analyzed as internal standard. Details of instrumental conditions and data acquisition were given in Hu et al. (2012a, b).

4.3 Bulk-rock major and trace elements

The bulk-rock major element oxides were analyzed using a Leeman Prodigy inductively coupled plasma-optical emission spectrometer (ICP-OES) at China University of

Geosciences, Beijing. Precisions (1σ) for most elements based on rock standards GSR-1, GSR-3 (National Geological Standard Reference Materials of China) and AGV-2 (US Geological Survey) are better than 1.0% except for TiO_2 (<1.5%) and P_2O_5 (1.0-1.5%). Loss on ignition (LOI) was determined by placing 500 mg of samples in a muffle furnace at 1000 °C for several hours before cooled in a desiccator and reweighed.

Bulk-rock trace elements concentrations were determined using an Agilent 7700e ICP-MS in the Wuhan SampleSolution Analytical Technology Co., Ltd. The rock powder (~50 mg) was dissolved in a Teflon bomb using a mixture HF and HNO_3. The Teflon bomb was put in a stainless-steel pressure jacket and heated to 190 °C in an oven for >24 h. After cooling, the Teflon bomb was opened and placed on a hotplate at 140 °C and evaporated to dryness. The dried sample was refluxed with 1 ml of HNO_3. The final solution was diluted to ~100 g with 2% HNO_3 in a polyethylene bottle. Detailed operating conditions of the ICP-MS instrument and data reduction have been described by Liu et al. (2008).

4.4 Bulk-rock Sr-Nd-Pb-Mg isotopes

Rock powders were dissolved using a mixture of concentrated HF and HNO_3 in Teflon beakers in Isotope Geochemistry and Geochronology Research Centre, Carleton University (IGGRC-CU), followed by 8 M HNO_3 and 6 M HCl. Sr, Nd and Pb were separated following the ion exchange column procedures described in Cousens (1996). Isotopes were measured using a Thermo-Finnigan Neptune MC-ICP-MS. Sr and Nd isotopic ratios were normalized against $^{86}Sr/^{88}Sr = 0.1194$ and $^{146}Nd/^{144}Nd = 0.7219$, respectively. Thallium was used as an internal standard to correct for instrumental drift on Pb isotopes; the measured $^{143}Nd/^{144}Nd$ ratios for the samples were corrected for the offsets of the measured JNdi values against a reference value of 0.512115 (Tanaka et al., 2000). Pb isotope ratios were corrected for the

offsets of measured NBS981 values against the reference values of Todt et al. (1996). Measurements of USGS rock standard BCR-2 and NBS987 yield average $^{87}Sr/^{86}Sr$ ratios of 0.705019 (n=3) and 0.710258 ± 0.000025 (2SD, n=13), respectively, while the average $^{143}Nd/^{144}Nd$ ratios of BCR-2 and international standard JNdi-1 are 0.512640 ± 0.000008 (n=1) and 0.512088 ± 0.000013 (2SD, n=18), respectively. NBS981 bracketing the samples, yields average ratios of $^{206}Pb/^{204}Pb$ = 16.9317 ± 0.0012 (2SD, n=16), $^{207}Pb/^{204}Pb$ = 15.4853 ± 0.11 (2SD, n=16), and $^{208}Pb/^{204}Pb$ = 36.6784 ± 0.0035 (2SD, n=16). Analysis of BCR-2 yields $^{206}Pb/^{204}Pb$ = 18.7579, $^{207}Pb/^{204}Pb$ = 15.6173, and $^{208}Pb/^{204}Pb$ = 38.7226. The total procedure blanks are <100, <250 and <50 pg for Pb, Sr and Nd respectively.

The Mg isotopic analysis, using the sample-standard bracketing method, was conducted using a *Nu Plasma II* HR MC-ICP-MS at the Isotope Laboratory of the University of Washington following the established protocols (Teng et al., 2007, 2010). Rock powders were dissolved in screw-top beakers using a 3:1 (v/v) mixture of Optima grade HF and HNO_3 acids. These capped beakers were heated at 70-80 °C, and then the solutions were evaporated to dryness. The dried samples were refluxed with a 3:1 (v/v) mixture of HCl and HNO_3, and then evaporated again to achieve 100% dissolution. The residues were then dissolved in 1 N HNO_3 for chromatographic separation. Separation of Mg was achieved using cation exchange columns loaded with 1 ml pre-cleaned resin (BioRad 200-400 mesh AG50W-X8). The Mg yields range from 99.5% to 99.9%. Samples were passed through the columns twice to achieve the required level of purification. The analytical results for magnesium isotopes are expressed as δ-notation in per mil relative to DSM3: $\delta^{X}Mg = [(^{X}Mg/^{24}Mg)_{sample}/(^{X}Mg/^{24}Mg)_{DSM3} - 1] \times 1000$, where X refers to mass 25 or 26 and DSM3 is a magnesium solution made from pure Mg metal (Galy et al., 2003). The standard materials San Carlos olivine, Hawaiian seawater, BHVO-1 and G-2 were processed during sample analyses. Their results agree with published values (Teng et al., 2015).

5 Results

5.1 Mineral chemistry

Plagioclase is common in most igneous rocks with varying compositions. To better understand the magmatic processes, EPMA is used to analyze the composition of plagioclase in both host tonalite and mafic enclaves (SQ1631 and SQ1609, Fig.4,5).

The plagioclase from the tonalite (SQ1631) is bytownite (An_{75-87}, Fig.4) with a core-to-rim An decrease (Fig.5a,b). Plagioclase in the enclave (SQ1609) is mainly labradorite with An_{46-59} (Fig.4) and shows a symmetric and rhythmic zoning pattern, i.e., An increases from the core, and then decreases towards the rim (Fig.5c,d,e,f).

5.2 Zircon U-Pb ages and Hf isotopes

Zircons from the tonalite host and enclaves are euhedral to subhedral with magmatic oscillatory zoning in CL images (Fig.6, cf. Hoskin and Schaltegger, 2003), some of which from the enclaves exhibit the diagnostic of re-melting (Fig.6e,f). Crystal lengths are 80-150 μm with varying length/width ratio of 1:1 to 2:1 (Fig.6). The concentration of U and Th of these zircons ranges from 94 to 502, and 74 to 666, respectively. The Th/U ratios range from 0.58 to 2.13.

Four tonalite samples yield weighted mean zircon U-Pb ages of 154 ± 1 Ma, 167 ± 1 Ma, 163 ± 1 Ma, 161 ± 1 Ma, respectively (Fig.7a,b,c,d). Two mafic enclaves yield zircon U-Pb ages of 158 ± 1 Ma and 163 ± 3 Ma, respectively (Fig.7e,f). In addition, one zircon crystal from sample SQ1637 also gives an ancient U-Pb age (Fig.6f), probably captured from the crustal basement.

In *situ* zircon Hf isotopic analysis was performed on three tonalite and one enclave samples (Fig.8). Zircons from two tonalite samples (SQ1624 and SQ1626) show concentrated $\varepsilon_{Hf}(t)$ values with individual analyses range from −15.9 to −14.2 and −15.8 to −13.1, respectively, giving a tight crustal model age (T_{DM}^{C}) of 2.1 to 2.2 Ga and 2.0 to 2.2 Ga. Zircons from one tonalite (SQ1640) and the enclave (SQ1637) give varying zircon $\varepsilon_{Hf}(t)$ values (−11.6 to −0.2 and −13.8 to −7.4, respectively), with T_{DM}^{C} model ages of 1.2 to 1.9 Ga and 1.7 to 2.1 Ga, respectively.

5.3 Bulk-rock geochemistry

In terms of bulk-rock major element compositions, the host granitoids are also classified as tonalite, but the enclaves would be termed as "gabbro" (Fig.9a). The latter is incorrect and should be classified as mafic diorite in terms of the petrology and petrographic definition. Gabbros are dominated by clinopyroxene and plagioclase, resulting from crystal accumulation during fractional crystallization of mantle derived basaltic magmas, but diorites are dominated by amphibole and plagioclase, resulting from crystal accumulation during fractional crystallization of andesitic magmas of crustal origin (e.g., oceanic crust or mafic continental crust). Thus, caution must be exercised when using bulk-rock compositions to classify coarse-grained igneous rocks of cumulate origin (i.e., they are NOT melt in composition). The abundant amphibole (low SiO_2 and high CaO and MgO) leads to the mafic enclaves named as "gabbro". The tonalites have narrow ranges of SiO_2(58.3-63.9 wt.%), MgO (2.5-5.3 wt.%), CaO (4.9-7.5 wt.%), K_2O (1.7-3.5 wt.%), TiO_2 (0.49-0.88 wt.%), TFe_2O_3 (5.3-8.2 wt.%) and A/CNK (0.82-1.03), and low DI (Differentiation Index, 47.8-64.7) (Fig.9b,c, 10a-d, Table 1), with high-K calc-alkaline and calc-alkaline affinity (Fig.9b,c,d).

The mafic enclaves have lower SiO_2 (51.0-56.0 wt.%) and higher MgO (5.3-10.6 wt.%) (Fig.10, Table 1).

In terms of bulk-rock trace element compositions. They are relatively enriched in large ion lithophile elements (LILEs, e.g., Rb, Th, and U) and relatively depleted in high field strength elements (HFSEs, e.g., Nb, Ta, and Ti), with moderate negative Eu anomalies (Eu/Eu* = 0.58-0.9, Fig.11). For some enclaves, the relative overall abundance levels of rare earth elements (REEs) are proportional to amphibole/plagioclase modal ratio and negative Eu anomaly with light REE depletion (Fig.11).

All the tonalite samples show a narrow range of $^{87}Sr/^{86}Sr$ (0.714838-0.718417) and $\varepsilon_{Nd}(t)$ (−14 to −11.3), with similar radiogenic Pb isotope compositions ($^{206}Pb/^{204}Pb$ = 18.927–18.936, $^{207}Pb/^{204}Pb$ = 15.746–15.764, $^{208}Pb/^{204}Pb$ = 39.257–39.798) (Fig.12a,b,c). The enclave sample has the isotopic compositions of $^{87}Sr/^{86}Sr$ = 0.713941, $\varepsilon_{Nd}(t)$ = −9.8, $^{206}Pb/^{204}Pb$ = 18.806, $^{207}Pb/^{204}Pb$ = 15.739, $^{208}Pb/^{204}Pb$ = 39.521 (Fig.12a,b,c).

Compared with mantle peridotite ($\delta^{26}Mg$ = −0.25 ± 0.04‰, Teng et al., 2010), the $\delta^{26}Mg$ values of bulk-rock tonalite samples in this study are more variable (−0.40 to −0.19‰, Fig.12d) than the enclaves (−0.33 to −0.18‰, Fig.12d). The latter shows restricted range close to the mantle values, but the tonalite samples display variations from the mantle values to the much lighter values that seem to define a positive $\delta^{26}Mg$ vs. SiO_2 trend (Fig.12d).

6 Discussion

6.1 Petrogenesis of the tonalite in the west central Lhasa subterrane

The tonalite samples have a narrow SiO_2 range (Fig.10) and a low and narrow DI values (48-65, Fig.9c). These observations are consistent with similar modal mineralogy of these samples. Using incompatible trace elements with different bulk solid/melt partition

coefficients could distinguish different magma processes (Schiano et al., 2010). The tonalite samples display a positive correlation between La/Sm and La (Fig.13), which would be traditionally interpreted as resulting from partial melting rather than fractional crystallization. However, as seen from the REE patterns in Fig. 11a,c, the positive La/Sm-La correlation is a simple reflection of REE systematics controlled by the modal mineralogy of the rock samples, i.e., largely determined by amphibole/plagioclase proportions. The important point is that neither the host tonalite nor MMEs are of melt composition, but both are mixture of cumulate crystals with entrapped melt. Specifically, the MMEs are cumulate of early liquidus phases dominated by amphibole plus plagioclase with minor trapped melt from the same magmatic system whereas the tonalite host comprises more evolved liquidus phases with abundant trapped melt (Niu et al., 2013; Chen et al., 2016).

Sr-Nd-Pb isotopic compositions of granitoids can be used to discuss the sources and magmatic processes. Phanerozoic granitoids that originated from juvenile crust have rather different initial Sr-Nd isotopic compositions compared to those from ancient crust (Mo et al., 2007, 2008, 2009; Niu et al., 2015). Juvenile crust generally show positive $\varepsilon_{Nd}(t)$ and low $(^{87}Sr/^{86}Sr)_i$ values, while ancient continental crust have negative $\varepsilon_{Nd}(t)$ and high $(^{87}Sr/^{86}Sr)_i$ (Chen and Arakawa, 2005). In addition, zircon Hf isotope analyses are widely used to trace the source regions of their host magmas, which can readily distinguish the host magmas resulting from remelting of the ancient mature crustal materials or involve newly-derived mantle material for net crustal growth (Kemp et al., 2006; Scherer et al., 2007; Zhu et al., 2011).

The tonalite samples have concentrated Sr-Nd-Pb isotopic compositions with negative bulk-rock $\varepsilon_{Nd}(t)$ and zircon $\varepsilon_{Hf}(t)$ values, similar to the S-type granites and gneisses in the Lhasa terrane (Liu et al., 2014, Fig.8, 12a,b,c), suggesting an ancient deep crustal source.

The tonalite samples have a wide span of zircon $\varepsilon_{Hf}(t)$ of −15.9 to −0.2, larger than 10 epsilon units (Fig.8). In the Sr-Nd isotopic mixing modelling, all the samples plot along the mixing curve between the Yanhu basalt and the ancient Lhasa basement (Fig.12a). These observations indicate the involvement of mantle-derived depleted material, which is best understood as resulting from deep crustal melting (ancient basement source) caused by underplating/intrusion of basaltic magmas with relative contributions of 50-70% basement material and 30-50% basaltic material in terms of Sr-Nd isotopes.

In terms of the mafic enclaves, four hypotheses have been proposed to explain the origin: (i) residual material, which unmixes from melting of source rock that gave rise to the granitic liquid (Barbarin and Didier, 1992; Collins et al., 2006); (ii) cognate fragments of cumulate minerals or early formed crystals from the host magma (e.g. Shellnutt et al., 2010); (iii) products of magma mixing, that a coeval mafic magma that intruded into the felsic magma chamber (e.g. Barbarin, 2005); and (iv) xenoliths (Maas et al., 1997).

The mafic enclaves in this study display an equigranular texture without a cumulate textures (Fig.3e,f), but the absence of the "classic" cumulate texture is not the reason to deny their cumulate origin because the classic cumulate texture cannot be developed or preserved because of the recrystallization of entrapped melt under plastic compaction and deformation (see Chen et al., 2016). The rather similar Sr-Nd-Pb isotopic compositions between the enclaves and the host tonalite (Fig.12a,b,c) support the cumulate origin of the enclaves crystallized at early stages of the same magmatic system. The isotope differences between the two, if any, reflect the varying extent of crustal assimilation during magma evolution in a crustal magma reservoir (magma chamber). The enclaves have a heavy Mg isotopic composition resembling the mantle values (Fig.12d) and the host tonalite samples have both mantle and lighter Mg isotope values, but the overall variation range is rather small for

granites and granitoids in a global context, reflecting Mg isotope heterogeneity of crustal lithologies (Li et al., 2010).

The varying zircon $\varepsilon_{Hf}(t)$ (−13.8 to −7.4, > 6 epsilon units, Fig.8) of the enclaves also implies the involvement of depleted material, most likely reflecting Hf isotope composition of primitive parental melts. Both the tonalite samples and mafic enclaves have anomalously high compatible element composition (Fig.10e,f), which is consistent with the importance of mantle derived basaltic magmas responsible for causing crustal melting and tonalitic magma generation as discussed above.

Studies suggest that light Mg isotope is prone to partition into liquid during chemical weathering and heavy Mg isotope will be left in the residue (cf. Li et al., 2010). However, Mg isotopic compositions do not change significantly in whole rocks during partial melting of the mantle and differentiation of basaltic magma (Teng et al., 2007, 2010) or granitic magma (Ke et al., 2016; Li et al., 2010; Liu et al., 2010a).

Metamorphic dehydration is important in subduction zones and can significantly fractionate fluid-mobile elements and their isotopes (Elliott, 2004). However, it is found that both orogenic eclogites and mafic granulites have similar Mg isotopic compositions to their inferred protoliths (Li et al., 2011; Teng et al., 2013). Li et al. (2014b) found that Mg isotopic compositions of metapelites do not change during prograde metamorphism, even though significant amount of fluids was lost. All these indicate that metamorphic dehydration does not produce measurable Mg isotopic changes (Teng, 2017). The absence of Mg isotope fractionation during partial melting, magmatic differentiation and metamorphic dehydration allows us use Mg isotopic compositions of sampled felsic and mafic rocks to discuss the nature of their source region.

Li et al. (2010) has systematically measured multiple types of upper crustal rocks including granites, loess and shales, as well as upper crustal composites. It is suggested that

Mg isotopic composition of the upper continental crust is highly heterogeneous with δ^{26}Mg ranging from −0.52 to +0.92 and has a weighted average of −0.22 (Li et al., 2010). The heterogeneous Mg isotopic compositions are results of source heterogeneity produced by incorporation of old crustal components with variable Mg isotopic compositions (Li et al., 2010). The Mg isotopic compositions of the lower continental crust are also heterogeneous, with δ^{26}Mg ranging from −0.72 to +0.19, and likely reflect their distinct source compositions that involve preexisting, isotopically heterogeneous crustal materials (Teng et al., 2013).

To characterize the Mg isotopic composition of the mantle, Teng et al. (2010) has measured Mg isotopes for a globally distributed, geochemically diverse set of peridotite xenoliths. These peridotites have identical Mg isotopic compositions, with an average δ^{26}Mg = −0.25 ± 0.04‰ (2SD), which is used to represent the average Mg isotopic composition of the mantle and bulk Earth (Teng, 2017). However, metasomatized mantle xenoliths (wehrlites and pyroxenites) have large Mg isotopic variations at both bulk-rock and mineral scales, with δ^{26}Mg ranging from −0.48 to −0.12 (Yang et al., 2009), which reflects Mg isotopic heterogeneity in their mantle sources (Teng, 2017). The most likely process responsible for the mantle heterogeneity is metasomatism of subcontinental lithospheric mantle by reactions with melts derived from the subducted slabs (Teng, 2017).

Samples in this study, including the tonalite and the enclaves, show varying δ^{26}Mg ranging from −0.40 to −0.18 (Fig.12d), with an average δ^{26}Mg = −0.27 ± 0.06‰ (2SD), consistent with the heterogeneous Mg isotopic compositions of the continental crust (Li et al., 2010; Teng et al., 2013). However, heterogeneous Mg isotopic compositions cannot effectively explain the discontinued positive correlation between δ^{26}Mg and SiO_2 (Fig.12d). Considering the mantle-like average δ^{26}Mg and the varying zircon $\varepsilon_{Hf}(t)$ of both the host tonalite and the enclaves. The most plausible scenario is the significance of basaltic magmas

derived from metasomatized mantle, whose underplating and intrusion caused the crustal melting for the magmas parental to the tonalite and enclaves we study.

Given the negligible Mg isotope fractionation during partial melting, magma differentiation and metamorphic dehydration, the average δ^{26}Mg of −0.27 of samples from this study can be considered as the average Mg isotopic composition of the magma source, i.e., the continental crust in the western segment of the Lhasa terrane.

6.2 Geodynamic and tectonic implications

Mesozoic magmatism is widespread in the Lhasa terrane. The Late Triassic-Early Jurassic magmatic rocks in the Lhasa terrane are dominantly high-K calc-alkalic and shoshonitic series, with minor medium-K calc-alkalic rocks (Zhu et al., 2011). They were emplaced at 205-178 Ma in the southern Lhasa subterrane (Chu et al., 2006; Ji et al., 2009; Zhang et al., 2007), 210-183 Ma in the central Lhasa subterrane (Zhang et al., 2007). The Middle-Late Jurassic magmatic rocks are predominantly exposed in the central Lhasa subterrane (Fig.1), high-K calc-alkalic, and metaluminous to peraluminous (Fig.9b,d), with negative zircon $\varepsilon_{Hf}(t)$ (Fig.8).

Magmatic rocks of Early Cretaceous are widespread in the Lhasa terrane (Wu et al., 2010; Zhu et al., 2011). The rocks in the central Lhasa subterrane are medium- to high-K calc-alkalic and metaluminous to peraluminous compositions of 143-111 Ma (Zhu et al., 2011). The rocks in the northern Lhasa subterrane are predominantly high-K calc-alkalic series of 131-109 Ma (Zhu et al., 2011). Although the contemporaneous rocks from the Gangdese batholiths in the southern Lhasa subterrane may have been eroded away owing to orogenic uplift and erosion (Wu et al., 2010), magmatic rocks of this period are also identified in the southern Lhasa subterrane, represented by the adakite-like andesites of *ca.*

137 Ma (Zhu et al., 2009), granitoids of 109-102 Ma (Wen et al., 2008; Ji et al., 2009), and the abundant 130-100 Ma detrital zircons from the Xigaze forearc basin strata sourced from the Gangdese arc (Wu et al., 2010).

Late Cretaceous magmatic rocks are widespread in the southern Lhasa subterrane, whereas the contemporaneous rocks in the central and northern Lhasa subterranes have been reported from only several locations (Zhao et al., 2008; Zhu et al., 2011). They are dominantly diorite and granodiorite, medium- to high-K calc-alkalic, metaluminous, with zircon U-Pb ages of 95-80 Ma (Ji et al., 2009; Wen et al., 2008a, 2008b; Zhu et al., 2011).

Three different geodynamic models have been proposed to explain the origin of this magmatism: a) low-angle northward subduction of the Neo-Tethyan Ocean along the Indus–Yarlung suture zones (DeCelles et al., 2007; Kapp et al., 2005, 2007); b) southward subduction of the Bangong–Nujiang Ocean (Zhu et al., 2009, 2011; Sui et al., 2013); and c) combined effects of both (a) and (b) (Yin and Harrison, 2000; Pan et al., 2012).

Flat or low-angle subduction is thought to have a broad zone of calc-alkaline arc magmatism that migrates from the coastal to the continental interior (Gutscher et al., 2000; Li and Li, 2007). However, as described above, the distribution of the Mesozoic calc-alkaline arc magmatism in the Lhasa terrane does not show such south-to-north age younging. Furthermore, the initial northward subduction of the Neo-Tethyan Ocean seafloor beneath the Lhasa terrane is predicted to be triggered by the Lhasa-Qiangtang collision at *ca.* 140 Ma (Niu et al., 2003; Sengör et al., 1988; Zhu et al., 2009, 2011). Yet, the southern edge of the Lhasa terrane had been a passive margin rather than a mature active continental margin with a subduction zone in the Late Triassic-Late Jurassic (Zhu et al., 2013). Thus, magmatic rocks emplaced in this time period in the Lhasa terrane cannot be attributed to the northward subduction of the Neo-Tethyan Ocean lithosphere. The Middle-Late Jurassic magmatism of

this study is thus a tectonic response to the southward subduction of the Bangong–Nujiang Ocean beneath the Lhasa terrane.

The Bangong-Nujing Ocean is closed via divergent double-sided subduction in the Early Cretaceous (Zhu et al., 2016). Subduction of the Bangong-Nujiang Ocean lithosphere beneath the Qiangtang terrane initiated in the Mid-Late Triassic (Zhu et al., 2013; Zeng et al., 2016). Southward subduction of the ocean lithosphere beneath the Lhasa terrane is triggered by the Lhasa-northern Australia collision at *ca.* 260 Ma (Sengör et al., 1988; Niu et al., 2003; Zhu et al., 2011). This southward subduction subsequently triggered Indus-Yarlung Zangbo back-arc spreading, and then separated the Lhasa terrane from northern Australia (Zhu et al., 2011, 2013). With continued divergent subduction, rollback of the southward subducting slab then broke off at *ca.* 113 Ma, signifying the final amalgamation between the Lhasa and Qiangtang terranes (Zhu et al., 2009; 2011).

The question is what may have caused the ancient continental crust melting. In the context of the tectonic evolution discussed above, we suggest that, with sustained southward subduction of the Bangong-Nujiang Ocean lithosphere, subducted sediments or slab-derived fluids have metasomatized and led to partial melting of the continental lithospheric mantle beneath the Lhasa terrane. With subsequent slab roll-back, more mantle-derived hot mafic melts underplated and intruded the ancient Lhasa crust, causing its partial melting and granitoid magma generation in the west central Lhasa subterrane (Fig.14).

Gao et al., (2021) has reported the early Jurassic magmatism in the Basum Co and Gongbo Gyamda area in the eastern part of central Lhasa subterrane. Different from tonalites and mafic enclaves in this study, the early Jurassic plutonic rocks in the east central Lhasa subterrane have more depleted Sr-Nd isotope compositions (Fig.12a). The $(^{87}Sr/^{86}Sr)_i$ of the granites range from 0.7102 to 0.7127, with $\varepsilon_{Nd}(t)$ values from -8.7 to -7.5. The gabbros and diorites from Basum Co are characterized by lower Sr isotope compositions with $(^{87}Sr/^{86}Sr)_i$

ratios of 0.7053-0.7060, and negative $\varepsilon_{Nd}(t)$ values of -4.2 ~ -2.5 (Gao et al., 2021). All these rocks plot along the Sr-Nd isotopic mixing modelling curve (Fig.12a). The mafic rocks were derived from a melt-modified subarc mantle, and the granitoids were generated by the melting of the ancient Lhasa continental crust (Gao et al., 2021).

These observations confirm our current understanding that input of mantle wedge mafic melts is essential in causing crustal melting and the early Jurassic felsic magmatism in the east and the middle-late Jurassic granitoid magmatism in the west central Lhasa subterrane in this study. Therefore, the Jurassic magmatism in the central Lhasa subterrane is migrating from the east to the west. It is also coinciding with the subsequent diachronous Lhasa-Qiangtang collision during the Cretaceous (cf. Kapp et al., 2007; Yin and Harrison, 2000; Zhang, 2004).

7 Conclusions

(1) The southward subduction of the Bangong-Nujiang Ocean lithosphere and subsequent slab rollback metasomatized the mantle wedge and the lithospheric mantle above.

(2) Underplating and intrusion of basaltic melts derived from such metasomatized mantle triggered the ancient Lhasa crustal melting, generating the crustal magmas parental to the granitoids of Mid-Late Jurassic in the west central Lhasa subterrane.

(3) The continental crust in the western segment of the Lhasa terrane has a mantle-like average Mg isotopic composition of $\delta^{26}Mg = -0.27 \pm 0.06‰$ (2SD).

Acknowledgements

The authors are indebted to Yong Zhang for his help with zircon U-Pb isotopic analysis. This study was funded by grants from National Key R & D Project of China

(2016YFC0600304). The authors are grateful for careful reviews by anonymous reviewers, which greatly helps us improve the paper.

Declaration of interest statement

The authors declare that they have no known competing financial interests or personal relationships that could have appeared to influence the work reported in this paper.

References

Barbarin, B., 2005. Mafic magmatic enclaves and mafic rocks associated with some granitoids of the central Sierra Nevada batholith, California: nature, origin, and relations with the hosts. Lithos 80, 155-177.

Barbarin, B., Didier, J., 1992. Genesis and evolution of mafic microgranular enclaves through various types of interaction between coexisting felsic and mafic magmas. Earth and Environmental Science Transactions of the Royal Society of Edinburgh 83, 145-153.

Cao, M., Qin, K., Li, G., Li, J., Zhao, J., Evans, N.J., Hollings, P., 2016. Tectono-magmatic evolution of Late Jurassic to Early Cretaceous granitoids in the west central Lhasa subterrane, Tibet. Gondwana Research 39, 386-400.

Chen, B., Arakawa, Y., 2005. Elemental and Nd-Sr isotopic geochemistry of granitoids from the West Junggar foldbelt (NW China), with implications for Phanerozoic continental growth. Geochimica Et Cosmochimica Acta 69, 1307-1320.

Chen, S.,Niu, Y.L., Li, J.Y., Sun, W.L., Zhang, Y., Hu, Y., Shao, F.L., 2016. Syncollisional adakitic granodiorites formed by fractional crystallization: insights from their enclosed mafic magmatic enclaves (MMEs) in the Qumushan pluton, North Qilian Orogen at the northern margin of the Tibetan Plateau. Lithos 248/251, 455-468.

Chu, M.-F., Chung, S.-L., Song, B., Liu, D., O'Reilly, S.Y., Pearson, N.J., Ji, J., Wen, D.-J., 2006. Zircon U-Pb and Hf isotope constraints on the Mesozoic tectonics and crustal evolution of southern Tibet. Geology 34, 745-748.

Chung, S.L., Chu, M.F., Zhang, Y.Q., Xie, Y.W., Lo, C.H., Lee, T.Y., Lan, C.Y., Li, X.H., Zhang, Q., Wang, Y.Z., 2005. Tibetan tectonic evolution inferred from spatial and temporal variations in post-collisional magmatism. Earth-Science Reviews 68, 173-196.

Collins, W.J., Wiebe, R.A., Healy, B., Richards, S.W., 2006. Replenishment, Crystal Accumulation and Floor Aggradation in the Megacrystic Kanmantoo Suite, Australia. Journal of Petrology 47, 2073-2104.

Cousens, B.L., 1996. Magmatic evolution of Quaternary mafic magmas at Long Valley Caldera and the Devils Postpile, California: Effects of crustal contamination on lithospheric mantle-derived magmas. Journal of Geophysical Research: Solid Earth 101, 27673-27689.

DeCelles, P.G., Kapp, P., Ding, L., Gehrels, G.E., 2007. Late Cretaceous to middle Tertiary basin evolution in the central Tibetan Plateau: Changing environments in response to tectonic partitioning, aridification, and regional elevation gain. Geological Society of America Bulletin 119, 654.

De la Roche, H., Leterrier, J., Grandclaude, P.,Marchal,M., 1980. A classification of volcanic and plutonic rocks using R1R2-diagram and major-element analyses — its relationships with current nomenclature. Chem. Geol. 29, 183–210.

Dong, X., Niu, Y., Zhang, Z., Tian, Z., He, Z., 2020. Mesozoic crustal evolution of southern Tibet: Constraints from the early Jurassic igneous rocks in the Central Lhasa terrane. Lithos 366, 105557.

Dong, X., Zhang, Z., Santosh, M., 2010. Zircon U-Pb Chronology of the Nyingtri Group, Southern Lhasa Terrane, Tibetan Plateau: Implications for Grenvillian and Pan-African

Provenance and Mesozoic-Cenozoic Metamorphism. The Journal of Geology 118, 677-690.

Elliott, T., 2004. Tracers of the Slab, Inside the Subduction Factory, pp. 23-45.

Fan, J.J., Niu, Y.L., Liu, Y.M., Hao, Y.J., 2021. Timing of closure of the Meso-Tethys Ocean: Constraints from remnants of a 141-135 ocean island within the Bangong-Nujiang suture zone, Tibetan Plateau. Geological Society of America Bulletin 133, 1875-1889.

Galy, A., Yoffe, O., Janney, P.E., Williams, R.W., Cloquet, C., Alard, O., Halicz, L., Wadhwa, M., Hutcheon, I.D., Ramon, E., Carignan, J., 2003. Magnesium isotope heterogeneity of the isotopic standard SRM980 and new reference materials for magnesium-isotope-ratio measurements. Journal of Analytical Atomic Spectrometry 18, 1352-1356.

Gao, L.-E., Zeng, L., Wang, H., Gao, J., Shang, Z., Zhao, L., Hou, K., Guo, C., Ma, X., 2021. Contrasting Sr-Nd-Hf isotope systematics in Early Jurassic magmatic rocks from the Lhasa terrane: Implications for the lithospheric architecture of the Lhasa terrane. Lithos, 106050.

Gutscher, M.-A., Maury, R., Eisen, J.-P., Bourdon, E., 2000. Can slab melting be caused by flat subduction? Geology 28, 535-538.

Hoskin, P.W.O., Schaltegger, U., 2003. The Composition of Zircon and Igneous and Metamorphic Petrogenesis. Reviews in Mineralogy and Geochemistry 53, 27-62.

Hu, Z., Liu, Y., Gao, S., Liu, W., Zhang, W., Tong, X., Lin, L., Zong, K., Li, M., Chen, H., Zhou, L., Yang, L., 2012a. Improved in situ Hf isotope ratio analysis of zircon using newly designed X skimmer cone and jet sample cone in combination with the addition of nitrogen by laser ablation multiple collector ICP-MS. Journal of Analytical Atomic Spectrometry 27, 1391-1399.

Hu, Z., Liu, Y., Gao, S., Xiao, S., Zhao, L., Günther, D., Li, M., Zhang, W., Zong, K., 2012b. A "wire" signal smoothing device for laser ablation inductively coupled plasma mass spectrometry analysis. Spectrochimica Acta Part B: Atomic Spectroscopy 78, 50-57.

Ji, W.-Q., Wu, F.-Y., Chung, S.-L., Li, J.-X., Liu, C.-Z., 2009. Zircon U-Pb geochronology and Hf isotopic constraints on petrogenesis of the Gangdese batholith, southern Tibet. Chemical Geology 262, 229-245.

Kapp, P., DeCelles, P.G., Gehrels, G.E., Heizler, M., Ding, L., 2007. Geological records of the Lhasa-Qiangtang and Indo-Asian collisions in the Nima area of central Tibet. GSA Bulletin 119, 917-933.

Kapp, P., Yin, A., Harrison, T.M., Ding, L., 2005. Cretaceous-Tertiary shortening, basin development, and volcanism in central Tibet. GSA Bulletin 117, 865-878.

Ke, S., Teng, F.-Z., Li, S.-G., Gao, T., Liu, S.-A., He, Y., Mo, X., 2016. Mg, Sr, and O isotope geochemistry of syenites from northwest Xinjiang, China: Tracing carbonate recycling during Tethyan oceanic subduction. Chemical Geology 437, 109-119.

Kemp, A.I.S., Hawkesworth, C.J., Paterson, B.A., Kinny, P.D., 2006. Episodic growth of the Gondwana supercontinent from hafnium and oxygen isotopes in zircon. Nature 439, 580-583.

Li, S.-M., Zhu, D.-C., Wang, Q., Zhao, Z.-D., Sui, Q.-L., Liu, S.-A., Liu, D., Mo, X.-X., 2014a. Northward subduction of Bangong–Nujiang Tethys: Insight from Late Jurassic intrusive rocks from Bangong Tso in western Tibet. Lithos 205, 284-297.

Li, W.-Y., Teng, F.-Z., Ke, S., Rudnick, R.L., Gao, S., Wu, F.-Y., Chappell, B.W., 2010. Heterogeneous magnesium isotopic composition of the upper continental crust. Geochimica Et Cosmochimica Acta 74, 6867-6884.

Li, W.-Y., Teng, F.-Z., Wing, B.A., Xiao, Y., 2014b. Limited magnesium isotope fractionation during metamorphic dehydration in metapelites from the Onawa contact aureole, Maine. Geochemistry, Geophysics, Geosystems 15, 408-415.

Li, W.-Y., Teng, F.-Z., Xiao, Y., Huang, J., 2011. High-temperature inter-mineral magnesium isotope fractionation in eclogite from the Dabie orogen, China. Earth and Planetary Science Letters 304, 224-230.

Li, Z.-X., Li, X.-H., 2007. Formation of the 1300-km-wide intracontinental orogen and postorogenic magmatic province in Mesozoic South China: A flat-slab subduction model. Geology 35, 179-182.

Liu, D., Zhao, Z.D., Zhu, D.C., Niu, Y.L., DePaolo, D.J., Harrison, T.M., Mo, X.X., Dong, G.C., Zhou, S., Sun, C.G., Zhang, Z.C., Liu, J.L., 2014. Postcollisional potassic and ultrapotassic rocks in southern Tibet: Mantle and crustal origins in response to India-Asia collision and convergence. Geochimica Et Cosmochimica Acta 143, 207-231.

Liu, S.-A., Teng, F.-Z., He, Y., Ke, S., Li, S., 2010a. Investigation of magnesium isotope fractionation during granite differentiation: Implication for Mg isotopic composition of the continental crust. Earth and Planetary Science Letters 297, 646-654.

Liu, Y., Gao, S., Hu, Z., Gao, C., Zong, K., Wang, D., 2010b. Continental and Oceanic Crust Recycling-induced Melt–Peridotite Interactions in the Trans-North China Orogen: U–Pb Dating, Hf Isotopes and Trace Elements in Zircons from Mantle Xenoliths. Journal of Petrology 51, 537-571.

Liu, Y., Hu, Z., Gao, S., Günther, D., Xu, J., Gao, C., Chen, H., 2008. In situ analysis of major and trace elements of anhydrous minerals by LA-ICP-MS without applying an internal standard. Chemical Geology 257, 34-43.

Ludwig, K.R., 2003. ISOPLOT 3.0: A Geochronological Toolkit for Microsoft Excel. Berkeley Geochronology Center Special Publication.

Maas, R., Nicholls, I.A., Legg, C., 1997. Igneous and Metamorphic Enclaves in the S-type Deddick Granodiorite, Lachlan Fold Belt, SE Australia: Petrographic, Geochemical and Nd-Sr Isotopic Evidence for Crustal Melting and Magma Mixing. Journal of Petrology 38, 815-841.

Mo, X.X., Dong, G.C., Zhao, Z.D., Zhu, D.C., Zhou, S., Niu, Y.L., 2009. Mantle input to the crust in southern Gangdese, Tibet, during the Cenozoic: zircon Hf isotopic evidence. Journal of Earth Science 20, 241-249.

Mo, X.X., Hou, Z.Q., Niu, Y.L., Dong, G.C., Qu, X.M., Zhao, Z.D., Yang, Z.M., 2007. Mantle contributions to crustal thickening in south Tibet in response to the India-Asia collision. Lithos 96, 225-242.

Mo, X.X., Niu, Y.L., Dong, G.C., Zhao, Z.D., Hou, Z.Q., Zhou, S., Ke, S., 2008. Contribution of syncollisional felsic magmatism to continental crust growth: A case study of the Paleogene Linzizong Volcanic Succession in southern Tibet. Chemical Geology 250, 49-67.

Niu, Y.L., Liu, Y., Xue, Q.Q., Shao, J.L., Chen, S., Duan, M., Guo, P.Y., Gong, H.M., Hu, Y., Hu, Z.X., Kong, J.J., Li, J.Y., Liu, J.J., Sun, P., Sun, W.L., Ye, L., Xiao, Y.Y., Zhang, Y., 2015. Exotic origin of the Chinese continental shelf: New insights into the tectonic evolution of the western Pacific and eastern China since the Mesozoic. Science Bulletin, 60, 1598-1616.

Niu, Y.L., Zhao, Z.D., Zhu, D.C., Mo, X.X., 2013. Continental collision zones are primary sites for net continental crust growth – A testable hypothesis. Earth-Science Reviews 127, 96-110.

Niu, Y., O'Hara, M.J., Pearce, J.A., 2003. Initiation of Subduction Zones as a Consequence of Lateral Compositional Buoyancy Contrast within the Lithosphere: a Petrological Perspective. Journal of Petrology 44, 851-866.

Pan, G., Wang, L., Li, R., Yuan, S., Ji, W., Yin, F., Zhang, W., Wang, B., 2012. Tectonic evolution of the Qinghai-Tibet Plateau. Journal of Asian Earth Sciences 53, 3-14.

Rickwood, P.C., 1989. Boundary lines within petrologic diagrams which use oxides of major and minor elements. Lithos 22, 247–263.

Scherer, E.E., Whitehouse, M.J., Münker, C., 2007. Zircon as a Monitor of Crustal Growth. Elements 3, 19-24.

Schiano, P., Monzier, M., Eissen, J.-P., Martin, H., Koga, K.T., 2010. Simple mixing as the major control of the evolution of volcanic suites in the Ecuadorian Andes. Contrib. Mineral. Petrol. 160, 297–312.

Searle, M.P., Elliott, J.R., Phillips, R.J., Chung, S.-L., 2011. Crustal–lithospheric structure and continental extrusion of Tibet. Journal of the Geological Society 168, 633-672.

Sengör, A., Cin, A., Rowley, D.B., Nie, S.Y., 1993. Space - time patterns of magmatism along the Tethy - sides. Journal of Geology.

Sengör, A.M.C., Altıner, D., Cin, A., Ustaömer, T., Hsü, K.J., 1988. Origin and assembly of the Tethyside orogenic collage at the expense of Gondwana Land. Geological Society, London, Special Publications 37, 119-181.

Shellnutt, J.G., Jahn, B.M., Dostal, J., 2010. Elemental and Sr–Nd isotope geochemistry of microgranular enclaves from peralkaline A-type granitic plutons of the Emeishan large igneous province, SW China. Lithos 119, 34-46.

Smith, J.V., 1974. Nomenclature and General Properties of Feldspars, Feldspar Minerals: Crystal Structure and Physical Properties 1. Springer Berlin Heidelberg, Berlin, Heidelberg, pp. 415–460.

Sui, Q.-L., Wang, Q., Zhu, D.-C., Zhao, Z.-D., Chen, Y., Santosh, M., Hu, Z.-C., Yuan, H.-L., Mo, X.-X., 2013. Compositional diversity of ca. 110Ma magmatism in the northern

Lhasa Terrane, Tibet: Implications for the magmatic origin and crustal growth in a continent–continent collision zone. Lithos 168-169, 144-159.

Sun, S.S., McDonough, W.F., 1989. Chemical and isotopic systematics of oceanic basalts: implications for mantle composition and processes. Geol. Soc. Lond. Spec. Publ. 42, 313.

Tafti, R., Lang, J., Mortensen, J., Oliver, J., Rebagliati, C., 2014. Geology and Geochronology of the Xietongmen (Xiongcun) Cu-Au Porphyry District, Southern Tibet, China. Economic Geology 109, 1967-2001.

Tanaka, T., Togashi, S., Kamioka, H., Amakawa, H., Kagami, H., Hamamoto, T., Yuhara, M., Orihashi, Y., Yoneda, S., Shimizu, H., Kunimaru, T., Takahashi, K., Yanagi, T., Nakano, T., Fujimaki, H., Shinjo, R., Asahara, Y., Tanimizu, M., Dragusanu, C., 2000. JNdi-1: a neodymium isotopic reference in consistency with LaJolla neodymium. Chemical Geology 168, 279-281.

Tang, J., Lang, X., Xie, F., Gao, Y., Li, Z., Huang, Y., Ding, F., Yang, H., Zhang, L., Wang, Q., Zhou, Y., 2015. Geological characteristics and genesis of the Jurassic No. I porphyry Cu–Au deposit in the Xiongcun district, Gangdese porphyry copper belt, Tibet. Ore Geology Reviews 70, 438-456.

Teng, F.-Z., 2017. Magnesium Isotope Geochemistry. Reviews in Mineralogy and Geochemistry 82, 219-287.

Teng, F.-Z., Li, W.-Y., Ke, S., Marty, B., Dauphas, N., Huang, S., Wu, F.-Y., Pourmand, A., 2010. Magnesium isotopic composition of the Earth and chondrites. Geochimica Et Cosmochimica Acta 74, 4150.

Teng, F.-Z., Li, W.-Y., Ke, S., Yang, W., Liu, S.-A., Sedaghatpour, F., Wang, S.-J., Huang, K.-J., Hu, Y., Ling, M.-X., Xiao, Y., Liu, X.-M., Li, X.-W., Gu, H.-O., Sio, C.K., Wallace, D.A., Su, B.-X., Zhao, L., Chamberlin, J., Harrington, M., Brewer, A., 2015.

Magnesium Isotopic Compositions of International Geological Reference Materials. Geostandards and Geoanalytical Research 39, 329-339.

Teng, F.-Z., Wadhwa, M., Helz, R.T., 2007. Investigation of magnesium isotope fractionation during basalt differentiation: Implications for a chondritic composition of the terrestrial mantle. Earth and Planetary Science Letters 261, 84-92.

Teng, F.-Z., Yang, W., Rudnick, R.L., Hu, Y., 2013. Heterogeneous magnesium isotopic composition of the lower continental crust: A xenolith perspective. Geochemistry, Geophysics, Geosystems 14, 3844-3856.

Todt, W., Cliff, R.A., Hanser, A., Hofmann, A.W., 1996. Evaluation of a 202Pb–205Pb Double Spike for High - Precision Lead Isotope Analysis.*, Earth Processes: Reading the Isotopic Code.

Tong, X., Zhao, Z., Niu, Y., Zhang, S., Cousens, B., Liu, D., Zhang, Y., Han, M., Zhao, Y., Lei, H., Shi, Q., Zhu, D.-C., Sheikh, L., Lutfi, W., 2019. Petrogenesis and tectonic implications of the Eocene-Oligocene potassic felsic suites in western Yunnan, eastern Tibetan Plateau: Evidence from petrology, zircon chronology, elemental and Sr-Nd-Pb-Hf isotopic geochemistry. Lithos 340-341, 287-315.

Volkmer, J.E., Kapp, P., Guynn, J.H., Lai, Q., 2007. Cretaceous-Tertiary structural evolution of the north central Lhasa terrane, Tibet. Tectonics 26.

Wang, Y., Tang, J., Wang, L., Duan, J., Danzhen, W., Li, S., Li, Z., 2017. Petrogenesis of Jurassic granitoids in the west central Lhasa subterrane, Tibet, China: the Geji example. International Geology Review 60, 1-17.

Wen, D.-R., Chung, S.-L., Song, B., Iizuka, Y., Yang, H.-J., Ji, J., Liu, D., Gallet, S., 2008a. Late Cretaceous Gangdese intrusions of adakitic geochemical characteristics, SE Tibet: Petrogenesis and tectonic implications. Lithos 105, 1-11.

Wen, D.-R., Liu, D., Chung, S.-L., Chu, M.-F., Ji, J., Zhang, Q., Song, B., Lee, T.-Y., Yeh, M.-W., Lo, C.-H., 2008b. Zircon SHRIMP U–Pb ages of the Gangdese Batholith and implications for Neotethyan subduction in southern Tibet. Chemical Geology 252, 191-201.

Wu, F.-Y., Ji, W.-Q., Liu, C.-Z., Chung, S.-L., 2010. Detrital zircon U–Pb and Hf isotopic data from the Xigaze fore-arc basin: Constraints on Transhimalayan magmatic evolution in southern Tibet. Chemical Geology 271, 13-25.

Yang, W., Teng, F.-Z., Zhang, H.-F., 2009. Chondritic magnesium isotopic composition of the terrestrial mantle: A case study of peridotite xenoliths from the North China craton. Earth and Planetary Science Letters 288, 475-482.

Yin, A., Harrison, T.M., 2000. Geologic Evolution of the Himalayan-Tibetan Orogen. Annual Review of Earth and Planetary Sciences 28, 211-280.

Zeng, M., Zhang, X., Cao, H., Ettensohn, F.R., Cheng, W., Lang, X., 2016. Late Triassic initial subduction of the Bangong-Nujiang Ocean beneath Qiangtang revealed: stratigraphic and geochronological evidence from Gaize, Tibet. Basin Research 28, 147-157.

Zhang, K.-J., 2004. Secular geochemical variations of the Lower Cretaceous siliciclastic rocks from central Tibet (China) indicate a tectonic transition from continental collision to back-arc rifting. Earth and Planetary Science Letters 229, 73-89.

Zhang, Y., Zhang, K., Li, B., Wang, Y., Wei, Q., Tang, X., 2007. Zircon SHRIMP U-Pb geochronology and petrogenesis of the plagiogranites from the Lagkor Lake ophiolite, Gerze, Tibet, China. Chinese Science Bulletin 52, 651-659.

Zhao, T., Zhou, M.-F., Zhao, J.-H., Zhang, K.-j., Chen, W., 2008. Geochronology and geochemistry of the c. 80 Ma Rutog granitic pluton, northwestern Tibet: Implications for the tectonic evolution of the Lhasa Terrane. Geol. Mag 145, 845-857.

Zhu, D.-C., Li, S.-M., Cawood, P.A., Wang, Q., Zhao, Z.-D., Liu, S.-A., Wang, L.-Q., 2016. Assembly of the Lhasa and Qiangtang terranes in central Tibet by divergent double subduction. Lithos 245, 7-17.

Zhu, D.-C., Zhao, Z.-D., Niu, Y., Dilek, Y., Hou, Z.-Q., Mo, X.-X., 2013. The origin and pre-Cenozoic evolution of the Tibetan Plateau. Gondwana Research 23, 1429-1454.

Zhu, D.C., Mo, X.X., Niu, Y., Zhao, Z.D., Wang, L.Q., Pan, G.T., Wu, F.Y., 2009. Zircon U–Pb dating and in-situ Hf isotopic analysis of Permian peraluminous granite in the Lhasa terrane, southern Tibet: Implications for Permian collisional orogeny and paleogeography. Tectonophysics 469, 48-60.

Zhu, D.C., Mo, X.X., Zhao, Z.D., Niu, Y., Wang, L.Q., Chu, Q.H., Pan, G.T., Xu, J.F., Zhou, C.Y., 2010. Presence of Permian extension- and arc-type magmatism in southern Tibet: Paleogeographic implications. Geological Society of America Bulletin 122, 979-993.

Zhu, D.C., Zhao, Z.D., Niu, Y.L., Mo, X.X., Chung, S.L., Hou, Z.Q., Wang, L.Q., Wu, F.Y., 2011. The Lhasa Terrane: Record of a microcontinent and its histories of drift and growth. Earth and Planetary Science Letters 301, 241-255.

Fig. 1 (a) Topographic map showing tectonic units and boundaries of the Tibetan plateau (modified from Searle et al., 2011; Tong et al., 2019, based on the Google Earth website); (b) Geological map showing outcrop distributions of the Mesozoic magmatism in the Lhasa Terrane (modified from Zhu et al., 2011, 2013; Cao et al., 2016; Dong et al., 2020; Gao et al. 2021), indicating the study area as “Fig. 2” rectangle. Abbreviation: ATF, Altyn Tagh Fault; KLF, Kunlun Fault; KF, Karakorum Fault; MBT, Main Boundary Thrust; JSZ, Jinsha suture zone; BNSZ, Bangong-Nujiang suture zone; IYZSZ, Indus-Yarlung Zangbo suture zone; SNMZ, Shiquan river-NamTso Mélange zone; LMF, Luobadui-Milashan Fault.

Fig. 2 Simplified geological map of the study area showing sample locations.

Fig. 3 (a-b) Closeup outcrop photographs of the tonalite with mafic enclaves; (c-f) Photomicrographs of the tonalite (c,d) and mafic enclaves (e,f) under plane polarized light (c,e) and cross-polarized light (d,f), respectively. Abbreviation: Amp, Amphibole; Bi, Biotite; Cpx, Clinopyroxene; Pl, Plagioclase; Q, Quartz.

Fig 4 Feldspar classification diagram (Smith, 1974).

Fig 5 Backscattered electron (BSE) images (a,c,e) and compositional variations of plagioclase from the tonalite and the mafic enclave samples.

Fig 6 Cathodoluminescence (CL) images of representative zircons from the tonalite and enclave samples for age dating and Hf isotope analysis. White and yellow dashed circles indicate the spots for LA-ICP-MS U-Pb age dating and Hf isotope analysis, respectively. Values of zircon U-Pb ages (Ma) and $\varepsilon_{Hf}(t)$ are given.

Fig 7 U-Pb concordia diagrams for zircons from the tonalite and mafic enclave samples.

Fig 8 Zircon $\varepsilon_{Hf}(t)$ vs. U-Pb ages of our data in comparison with the literature data (Zhu et al., 2011). The grey field represents the Hf isotope composition of the ancient Lhasa basement or magmatic rocks largely derived from, or highly influenced by, the basement. CHUR, Chondritic Uniform Reservoir.

Fig 9 (a) R2 vs. R1 diagram for rock classification (De la Roche et al., 1980); (b) K_2O vs. SiO_2 diagram (Rickwood, 1989); (c) A/CNK vs. differentiation index (DI); (d) A/NK vs. A/CNK.

Fig 10 SiO_2 variation diagrams for TiO_2 (a), TFe_2O_3 (b), MgO (c), CaO (d), Ni (e) and Cr (f), showing major and compatible element compositions of the tonalite and enclave samples. The samples with lower SiO_2, Cr, Ni imply more cumulate clinopyroxene.

Fig 11 Chondrite-normalized rare earth element (REE) and primitive-mantle-normalized trace element patterns of the tonalite and mafic enclave samples. Normalization data are from Sun and McDonough (1989).

Fig 12 (a) $(^{87}Sr/^{86}Sr)_i$ vs. $\varepsilon_{Nd}(t)$; (b) $^{206}Pb/^{204}Pb$ vs. $^{207}Pb/^{204}Pb$; (c) $^{206}Pb/^{204}Pb$ vs. $^{208}Pb/^{204}Pb$; (d) SiO_2 vs. $\delta^{26}Mg$. The grey field represents the average $\delta^{26}Mg$ of -0.25 and 2SD of 0.04 for the normal mantle (Teng et al., 2010). Literature data are from Wang et al. (2017), Gao et al. (2021). Data for Laguo Co Ophiolite, Yanhu basalts, ancient Lhasa basement, Himalayan basement, Yarlung Zangbo Ophiolite, S-type granites, gneiss in the Lhasa terrane, Bulk Silicate Earth (BSE) and enriched mantle components (EM I and EM II) are from Wang et al. (2017), Liu et al. (2014) and references therein. Northern Hemisphere Reference Line (NHRL): $^{207}Pb/^{204}Pb = 0.1084 \times {}^{206}Pb/^{204}Pb + 13.491$; $^{208}Pb/^{204}Pb = 1.209 \times {}^{206}Pb/^{204}Pb + 15.627$. All initial isotopic ratios are corrected to t=160 Ma.

Fig 13 La/Sm vs. La (ppm) (modified from Schiano et al., 2010).

Fig 14 Schematic illustration showing the development of the Middle-Late Jurassic magmatism in the west central Lhasa subterrane (modified from Li et al., 2014a; Zhu et al., 2016).

Table 1 Major element oxide (wt. %), trace element (ppm) and whole-rock Sr-Nd-Pb-Mg isotope compositions of the Middle-Late Jurassic tonalites and the mafic enclaves in the west central Lhasa subterrane.

No.	1	2	3	4	5	6	7	8	9
Sample	SQ1601	SQ1611	SQ1613	SQ1614	SQ1615	SQ1616	SQ1617	SQ1618	SQ1619
Latitude(N)	32°32'2.6"	32°32'39.4"	32°32'30.2"	32°32'45.7"	32°32'33.4"	32°34'24.9"	32°35'15.1"	32°32'29.7"	32°32'39.0"
Longitude(E)	80°34'46.3"	80°32'22.2"	80°31'43.8"	80°29'48.0"	80°29'19.0"	80°29'44.2"	80°30'46.5"	80°28'19.0"	80°27'4.6"
Lithology	Tonalite	Tonalite	Tonalite	Tonalite	Tonalite	Tonalite	Tonalite	Tonalite	Tonalite
SiO_2	58.45	62.27	62.33	63.91	62.15	58.32	61.47	63.17	61.27
TiO_2	0.88	0.56	0.62	0.49	0.56	0.68	0.60	0.58	0.58
Al_2O_3	16.10	15.49	15.01	14.98	15.10	16.26	15.27	15.27	15.14
TFe_2O_3	8.17	6.03	6.57	5.27	6.00	7.98	6.40	5.77	6.47
MnO	0.14	0.11	0.13	0.11	0.12	0.17	0.12	0.11	0.13
MgO	3.87	2.88	3.13	2.54	3.15	3.81	3.31	2.82	3.54
CaO	7.54	6.03	5.73	4.88	5.51	6.14	5.13	5.32	5.11
Na2O	1.89	2.41	2.21	2.14	2.23	2.09	2.12	2.22	2.25
K_2O	1.91	2.21	2.26	3.11	2.29	1.65	1.82	2.92	2.69
P_2O_5	0.19	0.17	0.15	0.09	0.11	0.16	0.12	0.15	0.13
LOI	1.25	0.93	1.15	1.53	1.28	1.97	2.88	1.36	1.78
TOTAL	100.39	99.09	99.29	99.39	99.10	99.23	99.24	99.69	99.10
A/CNK	0.85	0.89	0.91	0.93	0.97	0.99	1.03	0.92	0.95
$Mg^{\#}$	48.41	48.62	48.55	48.84	50.98	48.61	50.61	49.19	52.01
DI	48	58	58	65	58	50	57	61	59
Li	23.7	23.6	31.2	32.8	32.3	38.8	32.6	33.2	35.5
Be	1.69	1.90	2.10	1.76	1.82	1.68	1.70	1.98	1.80
Sc	25.2	19.1	18.9	15.8	19.1	24.0	19.2	16.6	20.9
V	203	133	144	114	137	167	147	124	149
Cr	31.9	23.0	23.9	20.5	31.2	31.1	35.0	22.2	35.2
Co	18.4	13.1	14.2	11.3	13.5	16.2	15.0	12.9	15.0
Ni	9.40	7.25	7.07	5.94	6.93	7.63	7.96	6.90	7.76
Cu	12.5	6.69	4.11	3.91	3.43	7.63	11.8	5.42	5.5
Zn	84.6	63.2	71.1	56.2	60.1	76.0	63.2	62.6	62.7
Ga	19.4	16.9	17.3	16.0	16.8	17.6	16.6	16.9	16.7
Rb	83.1	95.5	120	140	108	66.9	84.5	130	112
Sr	308	270	254	253	243	257	249	255	236
Y	28.6	24.9	25.1	22.3	21.9	29.8	18.6	23.5	23.2
Zr	152	102	132	124	148	133	117	141	117
Nb	9.52	9.40	10.5	9.14	8.71	9.57	10.0	9.99	9.42
Sn	2.52	2.16	2.47	1.91	1.73	1.96	1.34	2.06	2.00
Cs	4.89	3.44	5.32	5.06	5.96	3.63	4.30	4.46	5.81
Ba	377	304	214	451	285	259	271	355	350
La	27.1	10.5	17.5	51.7	28.8	22.4	28.9	28.3	27.6
Ce	61.6	29.4	36.8	94.9	56.7	52.6	53.6	55.4	54.8
Pr	7.42	4.08	4.49	9.03	6.04	6.26	5.48	6.10	5.98
Nd	29.2	18.1	18.5	29.8	21.6	24.7	19.3	22.4	22.1
Sm	5.98	4.43	4.43	4.87	4.14	5.19	3.65	4.45	4.53
Eu	1.33	1.00	0.96	1.05	0.94	1.10	0.86	0.98	0.97
Gd	5.64	4.36	4.39	4.04	3.74	4.82	3.24	3.99	4.00
Tb	0.85	0.71	0.70	0.63	0.62	0.83	0.53	0.66	0.65
Dy	5.29	4.37	4.18	3.89	3.92	5.11	3.25	4.02	3.96
Ho	1.00	0.89	0.87	0.76	0.75	1.06	0.67	0.81	0.82
Er	2.89	2.52	2.42	2.26	2.24	3.00	1.89	2.33	2.30

Tm	0.41	0.37	0.37	0.33	0.33	0.46	0.30	0.34	0.35
Yb	2.59	2.46	2.55	2.21	2.20	3.02	1.95	2.36	2.43
Lu	0.38	0.34	0.35	0.32	0.31	0.44	0.29	0.35	0.35
Hf	3.89	2.95	3.81	3.76	4.26	3.81	3.48	4.19	3.47
Ta	0.49	0.72	0.92	0.84	0.75	0.77	0.83	0.93	0.87
Tl	0.41	0.49	0.65	0.66	0.50	0.32	0.40	0.65	0.55
Pb	9.65	13.6	12.2	20.1	9.56	10.3	11.3	16.9	12.6
Th	4.85	4.10	7.39	31.6	16.9	10.6	15.4	15.8	16.3
U	0.63	0.78	1.36	1.09	1.59	1.21	1.56	1.31	2.16
Eu/Eu*	0.7	0.7	0.66	0.72	0.73	0.67	0.76	0.71	0.7
$(La/Yb)_N$	7.51	3.07	4.92	16.75	9.38	5.31	10.65	8.62	8.14
$\delta^{25}Mg$	-	-0.09	-0.11	-	-0.16	-	-	-0.11	-
$\delta^{26}Mg$	-	-0.21	-0.26	-	-0.35	-	-	-0.22	-
$^{87}Sr/^{86}Sr$	-	0.714838	-	-	-	-	-	-	-
$^{87}Sr/^{86}Sr(i)$	-	0.713184	-	-	-	-	-	-	-
$^{143}Nd/^{144}Nd$	-	0.511991	-	-	-	-	-	-	-
$^{143}Nd/^{144}Nd(i)$	-	0.511866	-	-	-	-	-	-	-
$\varepsilon Nd_{(t)}$	-	-11.3	-	-	-	-	-	-	-
$T_{DM}(Ga)$	-	2.03	-	-	-	-	-	-	-
$^{206}Pb/^{204}Pb$	-	18.93	-	-	-	-	-	-	-
$^{207}Pb/^{204}Pb$	-	15.746	-	-	-	-	-	-	-
$^{208}Pb/^{204}Pb$	-	39.257	-	-	-	-	-	-	-

No.	10	11	12	13	14	15	16	17	18
Sample	SQ1620	SQ1622	SQ1623	SQ1624	SQ1626	SQ1629	SQ1630	SQ1631	SQ1633
Latitude(N)	32°33'0.7"	32°33'8.1"	32°32'6.4"	32°32'44.3"	32°32'50.[illegible]"	32°21'29.2"	32°21'26.3"	32°21'48.5"	32°22'15.3"
Longitude(E)	80°25'12.1"	80°19'6.8"	80°15'43.8"	80°13'47.5"	[illegible]'36.3"	80°43'15.7"	80°43'16.1"	80°43'4.3"	80°42'38.0"
Lithology	Tonalite	Tonalite	Tonalite	Tonalite	Tonalite	Tonalite	Tonalite	Tonalite	Tonalite
SiO_2	62.96	62.14	60.15	61.[illegible]	60.74	61.59	61.53	61.36	63.01
TiO_2	0.56	0.61	0.64	[illegible].56	0.52	0.56	0.54	0.53	0.56
Al_2O_3	15.12	15.38	16.13	14.[illegible]	14.51	14.57	14.51	15.03	14.51
TFe_2O_3	6.01	6.09	6.10	6.23	6.29	6.23	6.05	6.07	6.10
MnO	0.12	0.11	0.11	0.12	0.13	0.11	0.11	0.12	0.11
MgO	3.01	3.67	3.88	4.[illegible]7	3.91	4.03	4.07	4.05	4.07
CaO	5.17	5.11	5.29	[illegible].49	6.14	5.87	5.54	6.13	5.53
Na2O	2.14	2.18	2.14	2.07	2.00	2.09	2.16	2.20	2.10
K_2O	2.93	2.69	2.33	2.26	2.40	2.55	2.55	2.32	2.49
P_2O_5	0.11	0.12	[illegible].15	0.11	0.14	0.10	0.11	0.09	0.11
LOI	1.10	1.18	[illegible].41	2.11	2.22	1.70	1.94	1.54	1.48
TOTAL	99.23	99.28	[illegible]9.3[illegible]	99.34	99.00	99.40	99.11	99.44	100.07
A/CNK	0.94	0.97	1.03	0.91	0.85	0.86	0.88	0.87	0.89
$Mg^{\#}$	49.80	54.42	[illegible].75	58.72	55.19	56.17	57.13	56.93	56.93
DI	61	59	56	56	56	57	58	55	58
Li	28.6	[illegible].4	33.0	18.8	16.4	24.8	25.3	23.6	26.8
Be	1.66	1.81	1.87	1.57	1.82	1.70	1.76	1.81	1.78
Sc	18.5	18.4	21.7	22.5	20.0	20.9	20.0	19.9	18.1
V	136	121	143	141	117	137	131	132	127
Cr	23.3	102	58.5	150	149	110	109	116	111
Co	13.0	14.1	14.6	16.3	14.7	16.0	15.8	17.8	17.7
Ni	5.38	18.6	12.4	22.3	26.3	21.8	22.1	27.7	29.1
Cu	4.74	7.99	7.8	4.36	3.02	12.3	12.6	19.6	19.6
Zn	55.4	63.7	57.0	55.1	74.4	56.1	51.4	65.1	62.8
Ga	15.9	16.9	17.0	15.6	15.9	16.5	16.2	16.1	16.6
Rb	120	115	98.3	92.2	101	110	104	98.4	109
Sr	233	185	199	186	206	224	214	206	216
Y	22.2	22.2	25.7	23.3	27.8	22.2	21.5	21.4	19.7
Zr	105	159	145	133	118	122	132	117	138
Nb	8.44	10.6	9.22	9.17	9.16	8.76	8.53	8.32	9.5
Sn	1.77	2.02	2.01	1.17	2.22	1.99	2.08	1.60	1.83
Cs	5.02	5.89	4.29	1.67	2.22	6.87	8.06	3.46	3.37
Ba	346	391	349	395	332	355	366	311	414
La	46.0	39.1	29.3	25.0	31.7	26.1	26.9	25.4	28.2
Ce	85.7	77.5	59.0	51.4	66.0	52.8	53.5	51.2	54.4
Pr	8.02	7.68	6.80	5.73	7.36	5.84	5.71	5.52	5.81
Nd	27.0	26.8	24.8	21.0	27.9	21.8	20.8	21.3	21.2
Sm	4.52	4.82	5.20	4.46	5.63	4.28	4.19	4.07	4.01

Eu	0.95	0.96	1.07	0.91	0.97	0.90	0.88	0.87	0.87
Gd	3.85	4.03	4.62	3.86	4.67	3.75	3.75	3.72	3.49
Tb	0.61	0.64	0.75	0.69	0.81	0.61	0.62	0.60	0.56
Dy	3.74	3.77	4.49	4.02	4.81	3.85	3.78	3.64	3.41
Ho	0.75	0.78	0.92	0.83	1.01	0.79	0.75	0.73	0.71
Er	2.16	2.25	2.64	2.35	2.74	2.22	2.18	2.11	1.97
Tm	0.32	0.33	0.40	0.36	0.42	0.32	0.33	0.30	0.30
Yb	2.31	2.24	2.60	2.37	2.84	2.23	2.21	2.11	2.00
Lu	0.33	0.34	0.39	0.37	0.41	0.33	0.32	0.31	0.29
Hf	3.11	4.51	4.27	3.78	3.42	3.50	3.68	3.28	3.73
Ta	0.79	0.92	0.77	0.78	0.77	0.72	0.69	0.65	0.73
Tl	0.58	0.59	0.52	0.45	0.56	0.58	0.55	0.51	0.56
Pb	11.9	17.7	11.3	11.9	17.2	15.9	15.5	20.9	16.3
Th	27.4	22.4	15.8	17.3	16.5	12.2	12.9	11.9	12.6
U	1.65	1.86	1.27	1.90	1.56	1.36	1.32	1.35	1.39
Eu/Eu*	0.7	0.66	0.67	0.67	0.58	0.69	0.68	0.68	0.71
$(La/Yb)_N$	14.26	12.51	8.06	7.58	8	8.39	8.71	8.62	10.09
$\delta^{25}Mg$	-0.11	-	-	-0.16	-0.14	-	-	-0.21	-0.11
$\delta^{26}Mg$	-0.19	-	-	-0.3	-0.3	-	-	-0.4	-0.21
$^{87}Sr/^{86}Sr$	-	-	-	0.718417	-	-	-	-	-
$^{87}Sr/^{86}Sr(i)$	-	-	-	0.715376	-	-	-	-	-
$^{143}Nd/^{144}Nd$	-	-	-	0.511851	-	-	-	-	-
$^{143}Nd/^{144}Nd(i)$	-	-	-	0.511738	-	-	-	-	-
$\varepsilon Nd_{(t)}$	-	-	-	-13.8	-	-	-	-	-
$T_{DM}(Ga)$	-	-	-	2.01	-	-	-	-	-
$^{206}Pb/^{204}Pb$	-	-	-	18.936	-	-	-	-	-
$^{207}Pb/^{204}Pb$	-	-	-	15.764	-	-	-	-	-
$^{208}Pb/^{204}Pb$	-	-	-	39.798	-	-	-	-	-

No.	19	20	21	22	23	24	25	26	27
Sample	SQ1640	SQ1641	SQ1642	SQ1646	SQ1647	SQ1648	SQ1649	SQ1604	SQ1608
Latitude(N)	32°23'20.0"	32°23'20.0"	32°23'20.0"	32°25'[illegible]2"	32°25'29.6"	32°26'6.4"	32°26'3.9"	32°31'57.3"	32°31'58.9"
Longitude(E)	80°41'52.2"	80°41'52.2"	80°41'52.2"	80°26'1.1[illegible]	80°25'58.1"	80°26'2.6"	80°26'4.1"	80°34'29.9"	80°34'4.1"
Lithology	Tonalite	Tonalite	Tonalite	Tonalite	Tonalite	Tonalite	Tonalite	Mafic enclave	Mafic enclave
SiO_2	59.14	61.73	61.99	[illegible].16	61.00	60.93	61.91	52.25	51.04
TiO_2	0.60	0.56	0.55	0.54	0.59	0.58	0.56	1.00	1.01
Al_2O_3	15.06	14.57	14.[illegible]5	15.13	15.22	15.52	15.19	15.49	14.85
TFe_2O_3	7.25	6.16	[illegible].24	5.71	6.52	6.14	5.89	10.54	13.03
MnO	0.13	0.11	[illegible].12	0.11	0.12	0.12	0.11	0.21	0.23
MgO	5.31	4.25	3.9[illegible]	3.58	4.10	3.75	3.58	6.13	5.96
CaO	7.08	5.54	5.[illegible]4	5.75	5.88	5.85	5.69	8.87	8.71
Na2O	2.10	2.12	2.13	2.25	2.21	2.30	2.20	1.58	1.61
K_2O	1.88	2.4[illegible]	2.48	2.58	2.40	2.50	2.56	1.47	1.94
P_2O_5	0.12	[illegible].16	0.11	0.07	0.12	0.11	0.14	0.17	0.15
LOI	1.36	1.84	0.96	1.62	1.78	1.77	1.70	1.76	1.17
TOTAL	100.03	99.46	99.34	99.50	99.94	99.56	99.53	99.47	99.70
A/CNK	0.82	0.90	0.87	0.89	0.90	0.90	0.91	0.76	0.72
$Mg^{\#}$	59.20	57.75	55.76	55.40	55.47	54.73	54.63	53.54	47.54
DI	48	57	56	58	55	56	58	35	36
Li	22.4	19.2	17.2	25.7	27.2	16.9	25.3	28.1	25.9
Be	1.44	1.98	1.93	1.79	1.75	1.61	1.62	1.80	2.05
Sc	24.8	19.4	20.0	18.1	22.6	19.2	17.4	42.7	49.0
V	166	128	131	127	149	129	120	263	299
Cr	118	116	104	105	112	98.8	92.1	76.8	136
Co	18.2	16.2	16.7	14.1	16.7	15.9	14.1	28.9	27.5
Ni	18.4	27.3	27.9	21.3	22.9	24.3	19.6	11.8	17.4
Cu	10.8	11.3	12.0	9.87	13.1	13.1	8.87	30.5	33.0
Zn	63.4	60.2	65.6	61.6	63.9	58.0	61.5	102	118
Ga	16.8	16.8	17.4	16.7	17.0	16.8	16.0	20.5	20.9
Rb	88.0	101	114	106	96.8	109	106	53.0	72.4
Sr	199	217	210	205	192	218	203	249	225
Y	20.1	20.2	23.1	20.7	24.7	21.9	20.2	54.2	54.3
Zr	101	118	135	124	120	124	108	137	90.7
Nb	7.41	8.72	9.45	9.43	9.39	9.04	9.05	12.5	12.4
Sn	1.70	2.31	1.85	2.07	1.94	2.06	2.09	4.32	4.74
Cs	9.09	3.64	6.08	3.19	3.11	3.40	3.94	3.71	6.74

Ba	189	412	348	334	327	350	322	276	290
La	21.1	25.9	28.2	26.8	28.0	25.2	29.7	26.4	12.6
Ce	41.6	51.8	56.8	52.8	58.0	51.4	58.0	76.2	45.0
Pr	4.62	5.47	6.08	5.53	6.25	5.59	6.12	10.5	7.59
Nd	17.1	19.6	22.4	19.6	22.8	21.0	21.3	46.2	38.4
Sm	3.65	4.05	4.65	4.12	4.76	4.17	4.12	10.5	9.91
Eu	0.85	0.85	0.95	0.95	0.98	0.89	0.89	2.11	1.96
Gd	3.38	3.68	4.12	3.58	4.31	3.75	3.64	10.0	10.0
Tb	0.57	0.58	0.67	0.60	0.72	0.63	0.59	1.56	1.60
Dy	3.42	3.36	4.02	3.56	4.24	3.63	3.46	9.95	10.1
Ho	0.71	0.70	0.77	0.71	0.87	0.76	0.72	1.94	1.94
Er	2.06	1.99	2.30	2.08	2.48	2.13	1.95	5.42	5.39
Tm	0.31	0.30	0.34	0.30	0.37	0.33	0.31	0.81	0.78
Yb	2.05	1.95	2.25	2.04	2.44	2.15	2.03	5.19	5.13
Lu	0.31	0.31	0.34	0.32	0.38	0.33	0.31	0.73	0.70
Hf	3.07	3.30	3.79	3.42	3.39	3.37	3.06	3.84	2.90
Ta	0.71	0.73	0.77	0.75	0.78	0.67	0.76	0.59	0.58
Tl	0.44	0.57	0.60	0.53	0.47	0.64	0.65	0.29	0.37
Pb	13.5	19.7	16.4	18.3	14.1	13.1	23.9	5.69	7.20
Th	16.3	11.6	13.5	12.3	13.5	9.73	12.9	1.65	0.62
U	1.57	1.08	1.94	0.91	1.08	0.92	1.11	0.38	0.53
Eu/Eu*	0.74	0.67	0.67	0.75	0.67	0.6	0.7	0.63	0.6
$(La/Yb)_N$	7.38	9.5	8.96	9.41	8.23	8.38	10.52	3.64	1.77
$\delta^{25}Mg$	-0.18	-	-	-	-	-	-0.14	-0.12	-
$\delta^{26}Mg$	-0.36	-	-	-	-	-	-0.27	-0.27	-
$^{87}Sr/^{86}Sr$	0.718315	-	-	-	-	-	-	-	-
$^{87}Sr/^{86}Sr(i)$	0.715801	-	-	-	-	-	-	-	-
$^{143}Nd/^{144}Nd$	0.511853	-	-	-	-	-	-	-	-
$^{143}Nd/^{144}Nd$ (i)	0.51173	-	-	-	-	-	-	-	-
$\varepsilon Nd_{(t)}$	-14	-	-	-	-	-	-	-	-
$T_{DM}(Ga)$	2.23	-	-	-	-	-	-	-	-
$^{206}Pb/^{204}Pb$	18.927	-	-	-	-	-	-	-	-
$^{207}Pb/^{204}Pb$	15.763	-	-	-	-	-	-	-	-
$^{208}Pb/^{204}Pb$	39.797	-	-	-	-	-	-	-	-

No.	28	29	30	31	32	33	34
Sample	SQ1609	SQ1612	SQ1621	SQ1634	SQ1637	SQ1638	SQ1650
Latitude(N)	32°31'58.9"	32°32'40.2"	32°30'10.7"	32°22'15.3"	32°22'15.6"	32°22'15.6"	32°26'3.9"
Longitude(E)	80°34'4.1"	80°32'22.0"	80°29'12.1"	80°42'38.0"	80°42'38.2"	80°42'38.2"	80°26'4.1"
Lithology	Mafic enclave	Mafic enclave	Mafic enclave	Mafic enclave	Mafic enclave	Mafic enclave	Mafic enclave
SiO_2	55.53	52.63	52.07	55.80	54.63	56.00	54.62
TiO_2	0.77	0.85	0.69	0.59	0.56	0.27	0.57
Al_2O_3	12.68	16.4	17.34	13.61	14.31	9.93	13.68
TFe_2O_3	11.96	9.47	8.92	8.73	8.05	8.22	9.46
MnO	0.23	0.17	0.20	0.19	0.19	0.26	0.23
MgO	6.00	5.13	5.32	7.27	7.89	10.60	7.50
CaO	8.80	8.30	8.89	8.16	8.91	9.26	6.77
Na2O	1.45	2.18	2.30	2.30	2.43	1.90	2.81
K_2O	1.32	1.91	1.88	1.73	1.35	1.13	2.31
P_2O_5	0.12	0.10	0.15	0.08	0.09	0.07	0.09
LOI	0.83	1.54	1.73	1.35	0.96	1.76	1.73
TOTAL	99.69	99.38	99.49	99.81	99.37	99.41	99.77
A/CNK	0.64	0.76	0.79	0.66	0.66	0.47	0.70
$Mg^{\#}$	49.85	52.72	54.16	62.26	66.01	71.86	61.10
DI	39	40	39	42	38	35	46
Li	14.7	23.3	31.1	19.4	22.0	-	19.0
Be	1.85	1.51	1.57	1.99	1.53	-	1.44
Sc	44.2	30.7	25.6	30.6	30.7	-	29.6
V	231	249	197	182	190	-	182
Cr	251	29.8	14.6	345	346	-	469
Co	23.6	23.9	20.7	25.4	27.4	-	26.8
Ni	19.4	9.41	19.3	58.7	66.8	-	63.1
Cu	16.1	16.8	7.64	7.72	2.75	-	14.6
Zn	111	82.0	83.0	84.1	79.6	-	92.4
Ga	18.1	18.3	18.3	16.3	15.6	-	16.3
Rb	32.8	79.9	87.5	73.7	61.3	-	99.3
Sr	168	271	276	186	196	-	214
Y	59.7	27.3	34.6	31.3	21.1	-	30.9
Zr	83.3	73.6	78.7	101	86.9	-	85.6

Nb	11.0	8.99	10.1	8.16	6.05	-	8.20
Sn	5.03	2.55	2.63	2.66	2.11	-	2.90
Cs	3.17	2.91	4.04	1.73	2.29	-	3.34
Ba	134	194	193	154	148	-	256
La	11.1	37.8	20.9	24.6	19.4		20.9
Ce	46.1	71.3	55.7	59.3	41.3	-	54.6
Pr	8.20	7.41	7.20	7.43	4.70	-	7.23
Nd	41.5	27.1	28.5	29.2	17.8	-	28.9
Sm	11.0	5.28	6.10	6.05	3.62	-	6.12
Eu	2.13	1.49	1.38	1.26	1.05	-	1.37
Gd	11.2	5.06	5.51	5.28	3.52	-	5.28
Tb	1.73	0.79	0.94	0.85	0.58	-	0.89
Dy	11.0	4.85	5.80	5.32	3.56	-	5.12
Ho	2.11	0.97	1.22	1.08	0.72	-	1.08
Er	5.91	2.71	3.44	3.17	2.13	-	3.00
Tm	0.86	0.43	0.56	0.48	0.32	-	0.47
Yb	5.65	2.78	3.70	3.17	2.11	-	3.17
Lu	0.77	0.38	0.56	0.47	0.30	-	0.47
Hf	2.81	2.46	2.86	3.20	2.42	-	2.74
Ta	0.52	0.66	0.78	0.73	[illegible]	-	0.64
Tl	0.19	0.44	0.44	0.37	[illegible]	-	0.60
Pb	7.42	5.13	9.13	16.2	15.[illegible]	-	13.3
Th	0.39	3.75	7.80	10.5	6.8[illegible]	-	6.46
U	0.47	0.62	1.41	1.28	0.97	-	0.70
Eu/Eu*	0.59	0.88	0.73	0.68	0.9	-	0.74
$(La/Yb)_N$	1.41	9.77	4.05	5.55	6.6	-	4.72
$\delta^{25}Mg$	-0.14	-0.16	-	-0.1[illegible]	-0.14	-	-0.08
$\delta^{26}Mg$	-0.27	-0.33	-	-0.[illegible]4	-0.26	-	-0.18
$^{87}Sr/^{86}Sr$	-	0.713941	-	-	-	-	-
$^{87}Sr/^{86}Sr(i)$	-	0.711783	-	-	-	-	-
$^{143}Nd/^{144}Nd$	-	0.512053	-	-	-	-	-
$^{143}Nd/^{144}Nd(i)$	-	0.511941	-	-	-	-	-
$\varepsilon Nd_{(t)}$	-	-9.8	-	-	-	-	-
$T_{DM}(Ga)$	-	1.68	-	-	-	-	-
$^{206}Pb/^{204}Pb$	-	18.806		-	-	-	-
$^{207}Pb/^{204}Pb$	-	15.739	-	-	-	-	-
$^{208}Pb/^{204}Pb$	-	39.521	-	-	-	-	-

All initial isotopic ratios are corrected to t=160 Ma

Graphical abstract

Highlights

- The Jurassic magmatism in the west central Lhasa subterrane occurred at *ca.* 160 Ma.
- The southward subducted oceanic crust caused melting of the Lhasa continental crust.
- The average $\delta^{26}Mg$ of the continental crust of the Lhasa terrane is −0.27.

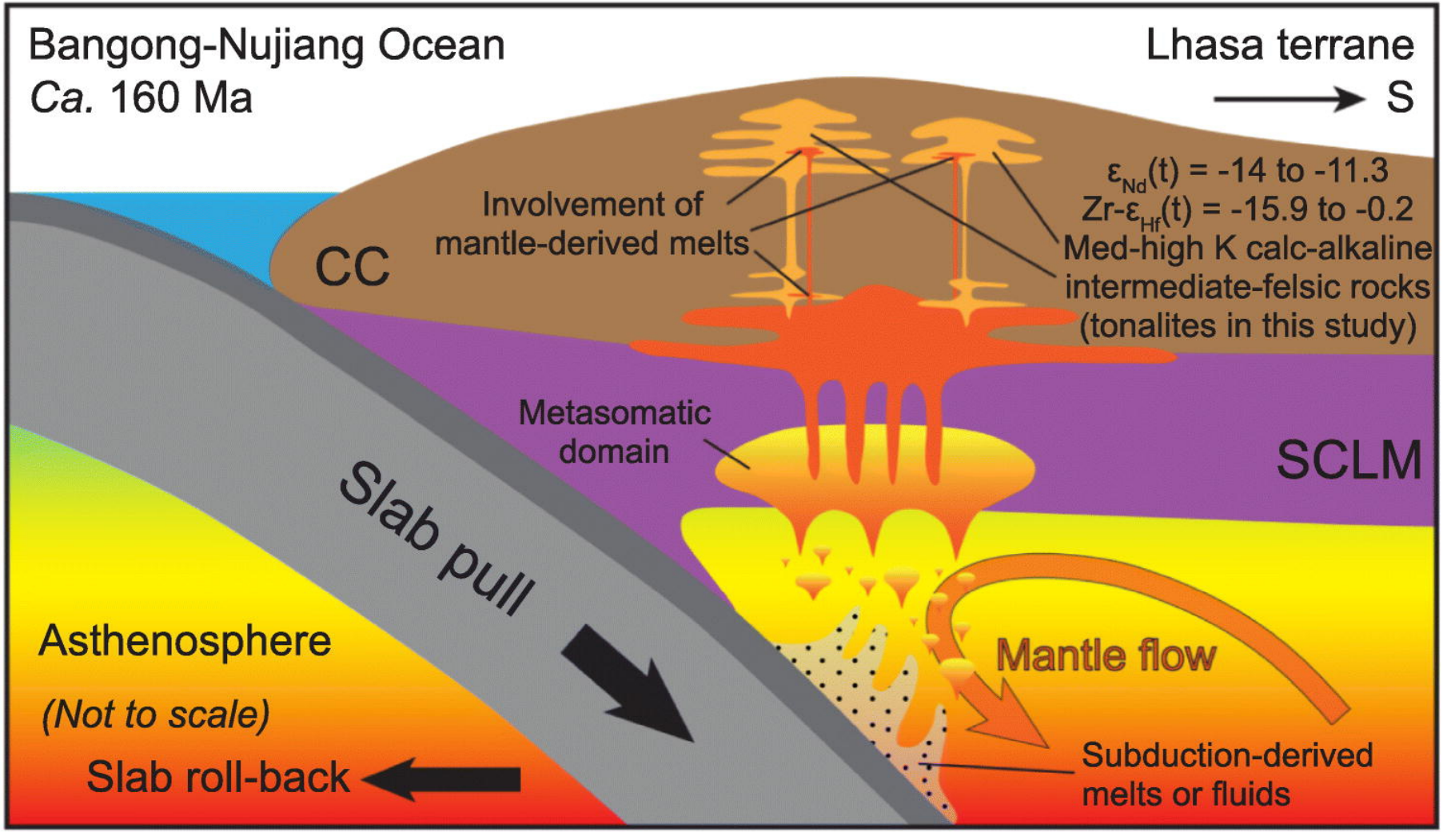

Graphics Abstract

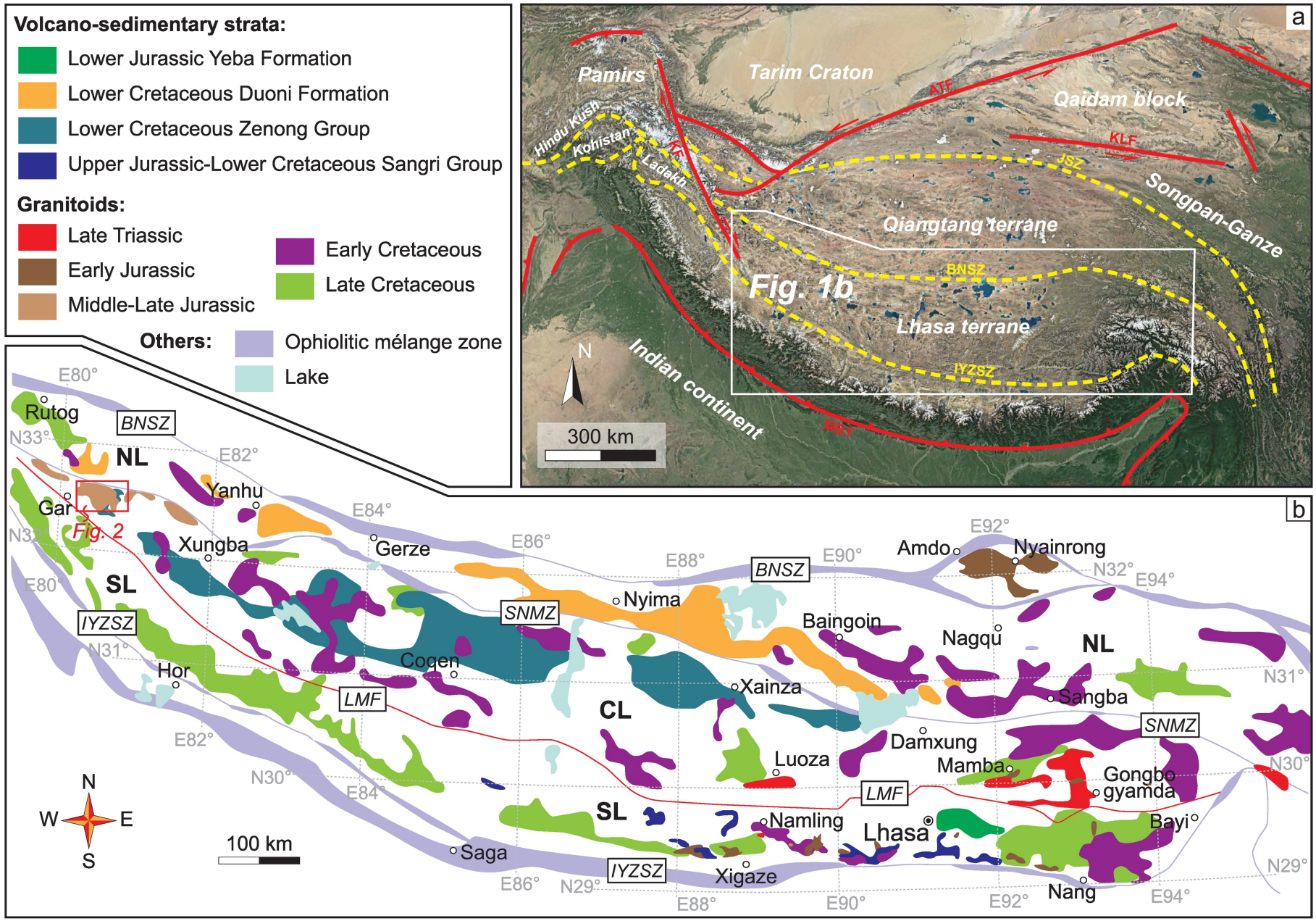
Volcano-sedimentary strata:
Lower Jurassic Yeba Formation
Lower Cretaceous Duoni Formation
Lower Cretaceous Zenong Group
Upper Jurassic-Lower Cretaceous Sangri Group
Granitoids:
Late Triassic
Early Jurassic
Middle-Late Jurassic
Early Cretaceous
Late Cretaceous
Others:
Ophiolitic mélange zone
Lake
a
Pamirs
Tarim Craton
ATF
Qaidam block
Hindu Kush
Kohistan
KF
Ladakh
KLF
JSZ
Songpan-Ganze
Qiangtang terrane
BNSZ
Fig. 1b
Lhasa terrane
IYZSZ
N
Indian continent
MBT
300 km
b
E80°
Rutog
BNSZ
N33°
NL
E82°
Yanhu
Gar
E84°
Fig. 2
N32°
Xungba
Gerze
E86°
E88°
BNSZ
E90°
Amdo
E92°
Nyainrong
N32°
E94°
E80°
SL
Nyima
SNMZ
Baingoin
Nagqu
NL
IYZSZ
N31°
Hor
Cogen
Xainza
N31°
LMF
CL
Sangba
E82°
SNMZ
Damxung
Luoza
Mamba
N30°
N30°
Gongbo
gyamda
E84
LMF
SL
Namling
Lhasa
Bayi
N
W
E
S
100 km
Saga
IYZSZ
Xigaze
N29°
E86°
N29°
Nang
E88°
E90°
E92°
E94°

Figure 1

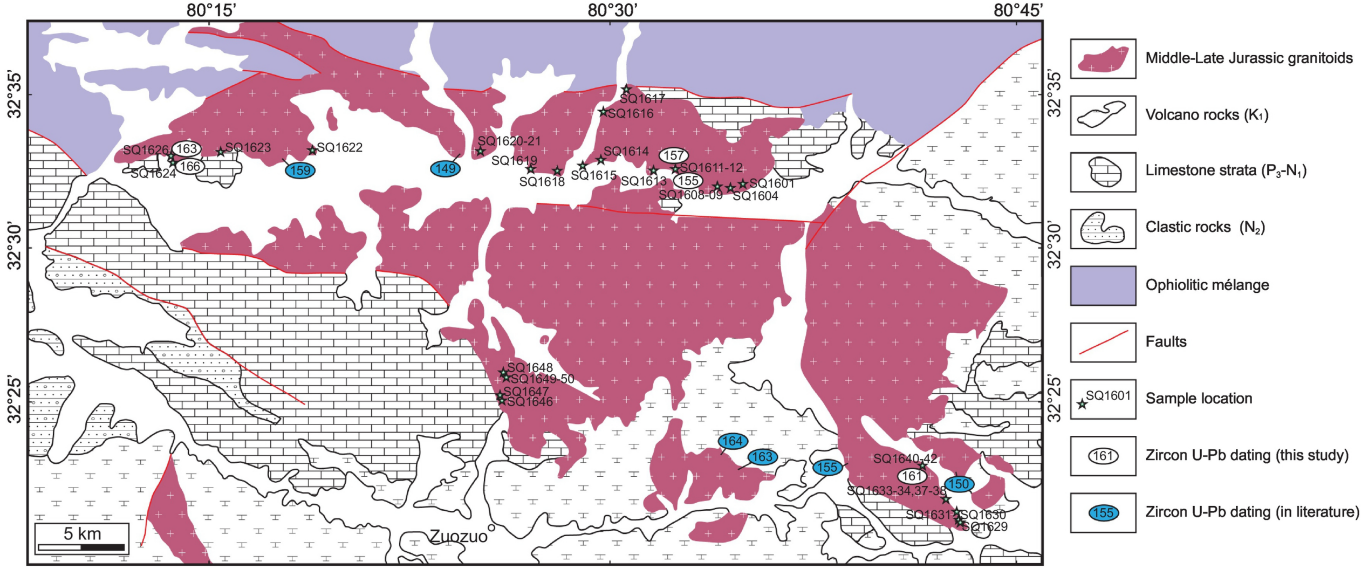
80°15'
80°30'
80°45'
32°35'
32°30'
32°25'
SQ1626
163
SQ1623
SQ1622
SQ1624
166
159
149
SQ1620-21
SQ1619
SQ1618
SQ1615
SQ1617
SQ1616
SQ1614
157
SQ1611-12
SQ1613
155
SQ1608-09
SQ1601
SQ1604
SQ1648
SQ1649-50
SQ1647
SQ1646
164
163
155
SQ1640-42
161
150
SQ1633-34,37-38
SQ1631
SQ1630
SQ1629
Zuozuo
5 km
Middle-Late Jurassic granitoids
Volcano rocks (K1)
Limestone strata (P3-N1)
Clastic rocks (N2)
Ophiolitic mélange
Faults
SQ1601
Sample location
161
Zircon U-Pb dating (this study)
155
Zircon U-Pb dating (in literature)

Figure 2

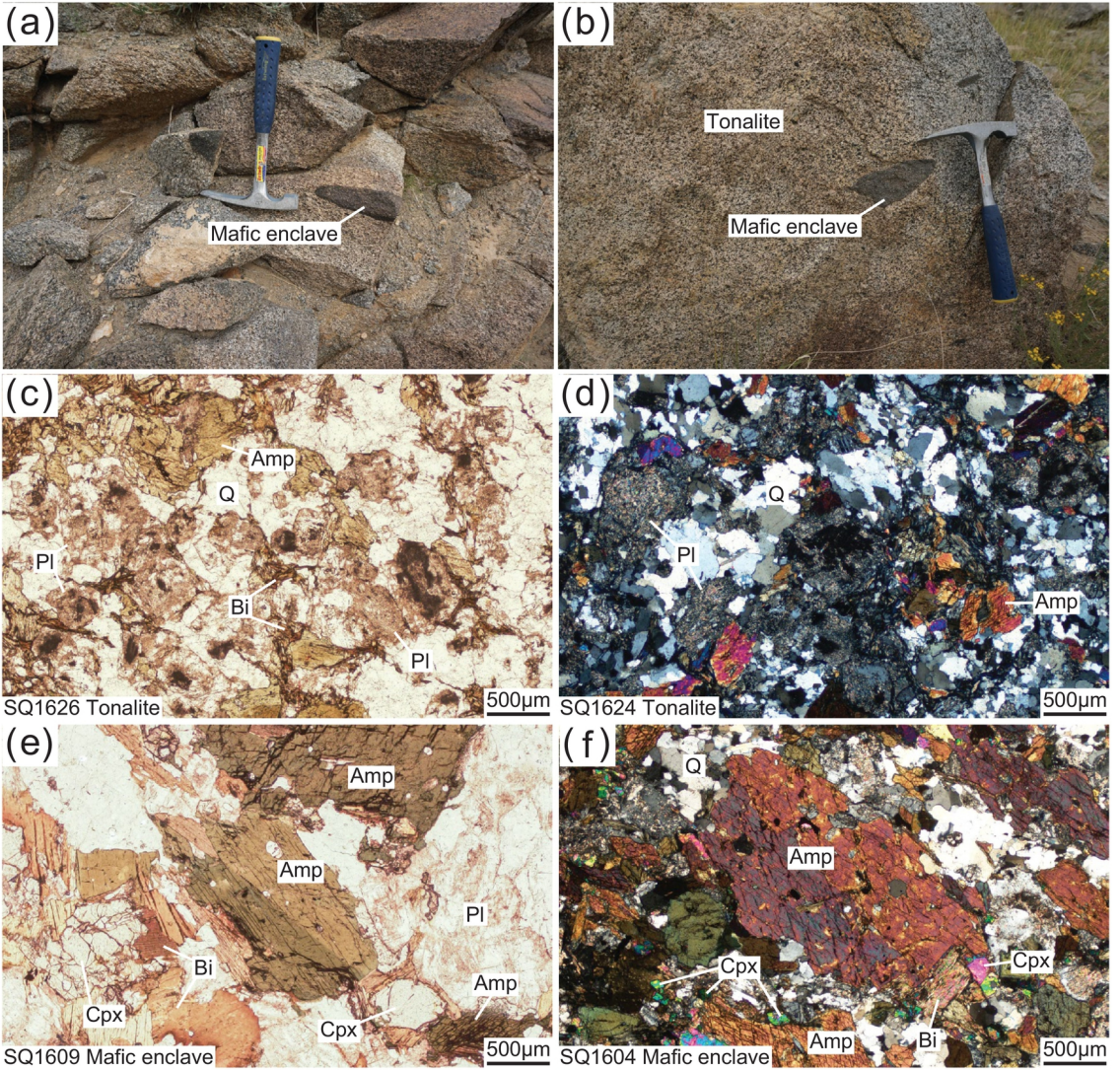
(a)
Mafic enclave
(b)
Tonalite
Mafic enclave
(c)
Amp
Q
Pl
Bi
Pl
SQ1626 Tonalite
500μm
(d)
Q
Pl
Amp
SQ1624 Tonalite
500μm
(e)
Amp
Amp
Pl
Bi
Amp
Cpx
Cpx
SQ1609 Mafic enclave
500μm
(f)
Q
Amp
Cpx
Cpx
Amp
Bi
SQ1604 Mafic enclave
500μm

Figure 3

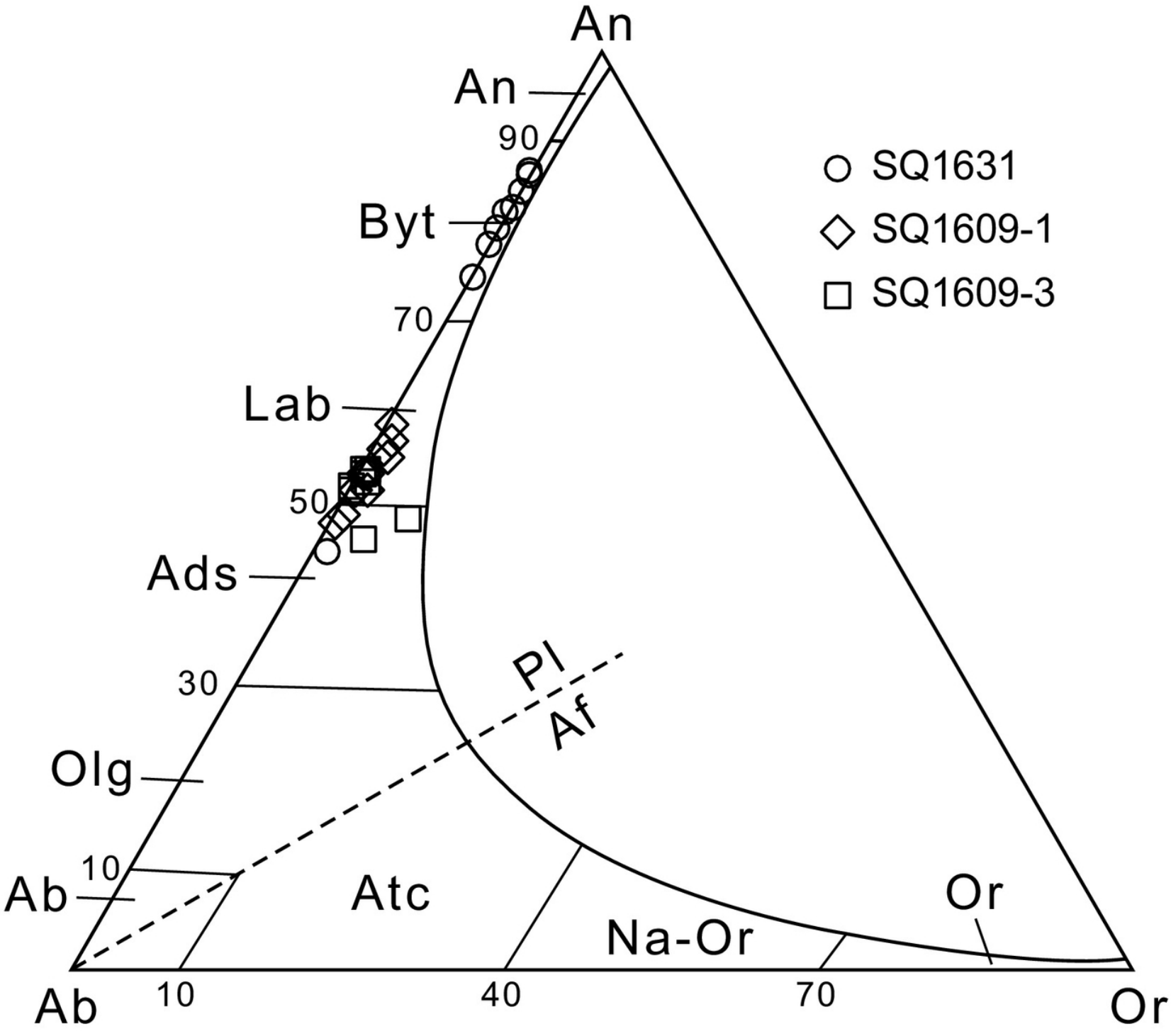
An
An
90
Byt
70
Lab
50
Ads
30
Olg
10
Ab
Ab
10
40
70
Or
Or
Pl
Af
Atc
Na-Or
SQ1631
SQ1609-1
SQ1609-3

Figure 4

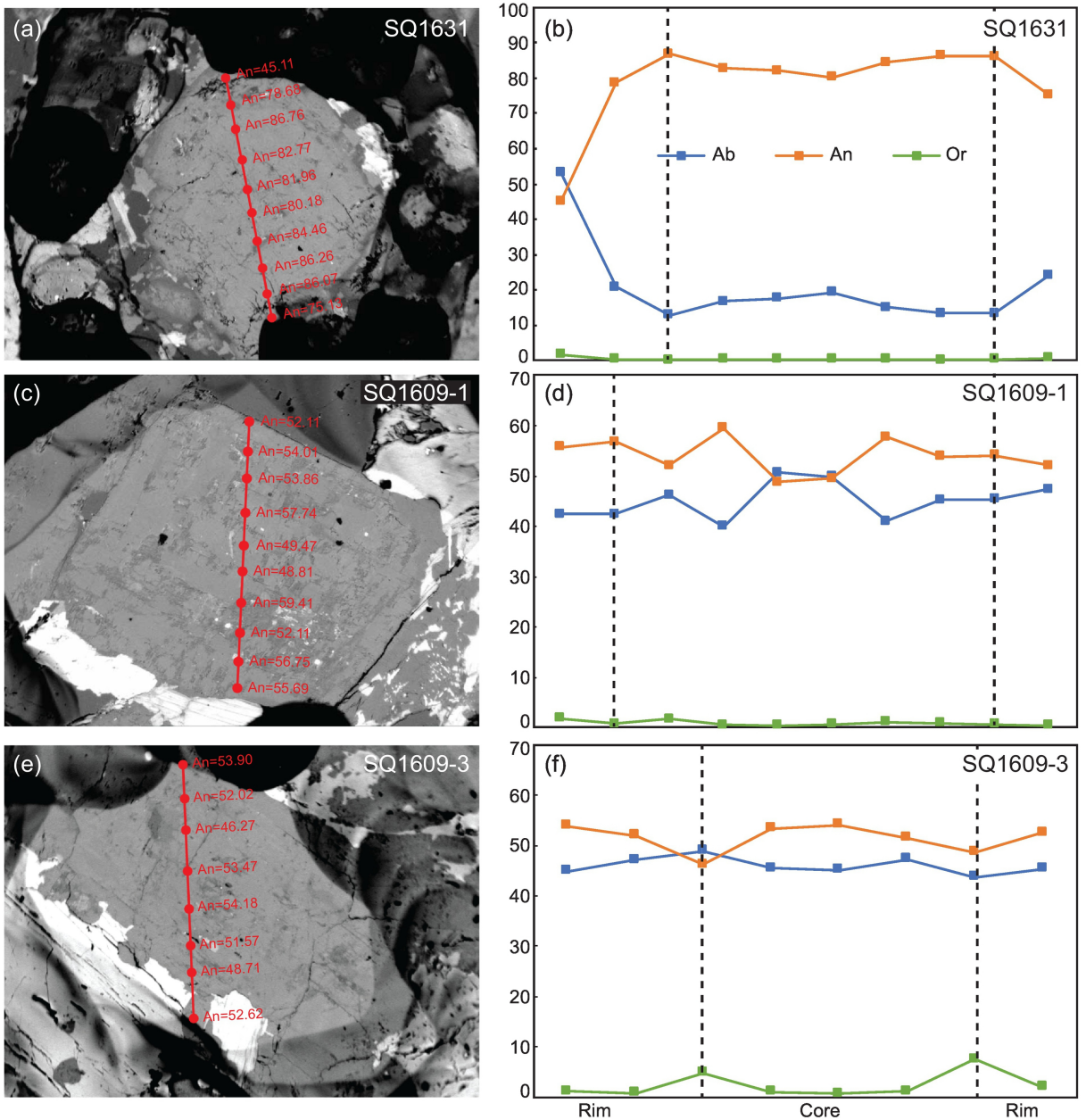
(a)
SQ1631
An=45.11
An=79.65
An=86.76
An=82.77
An=81.96
An=80.18
An=84.46
An=86.26
An=86.07
An=75.13
(b)
SQ1631
Ab
An
Or
(c)
SQ1609-1
An=52.11
An=54.01
An=53.86
An=57.74
An=49.47
An=48.81
An=59.41
An=52.11
An=56.75
An=55.69
(d)
SQ1609-1
(e)
SQ1609-3
An=53.90
An=52.02
An=46.27
An=53.47
An=54.18
An=51.57
An=48.71
An=52.62
(f)
SQ1609-3
Rim
Core
Rim

Figure 5

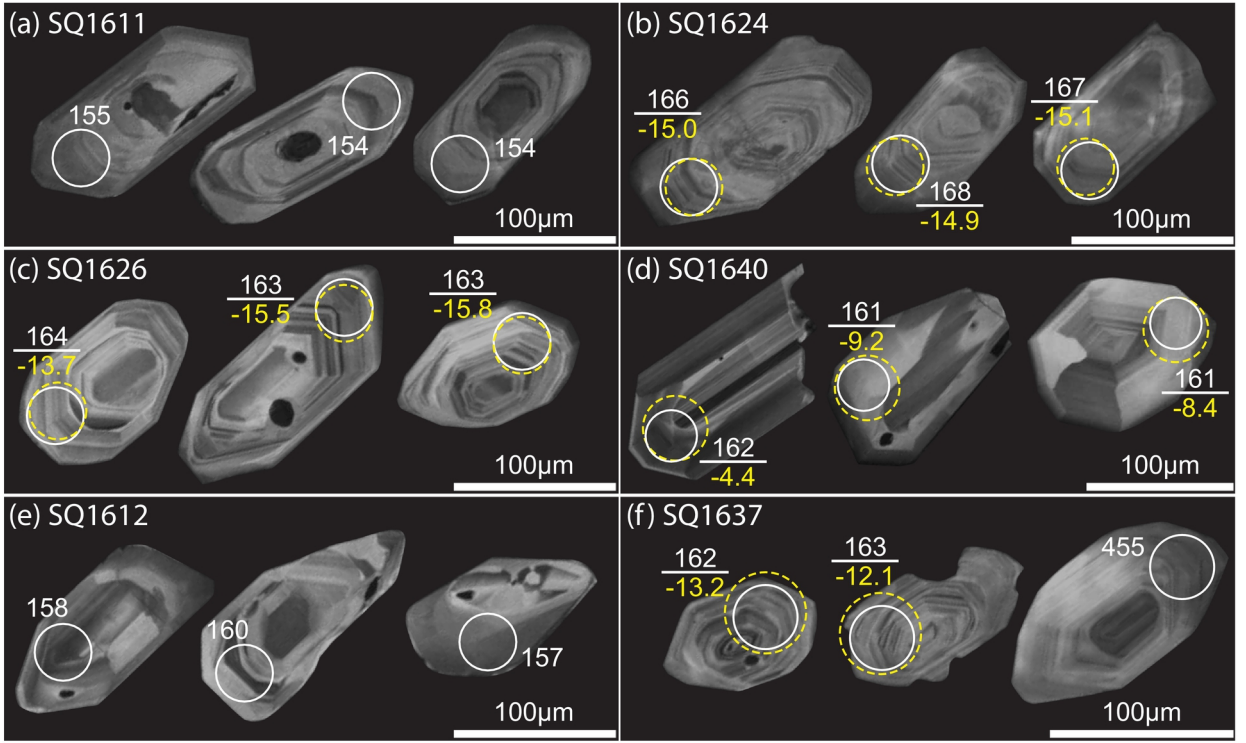
(a) SQ1611
155
154
154
100μm
(b) SQ1624
166
-15.0
168
-14.9
167
-15.1
100μm
(c) SQ1626
164
-13.7
163
-15.5
163
-15.8
100μm
(d) SQ1640
161
-9.2
162
-4.4
161
-8.4
100μm
(e) SQ1612
158
160
157
100μm
(f) SQ1637
162
-13.2
163
-12.1
455
100μm

Figure 6

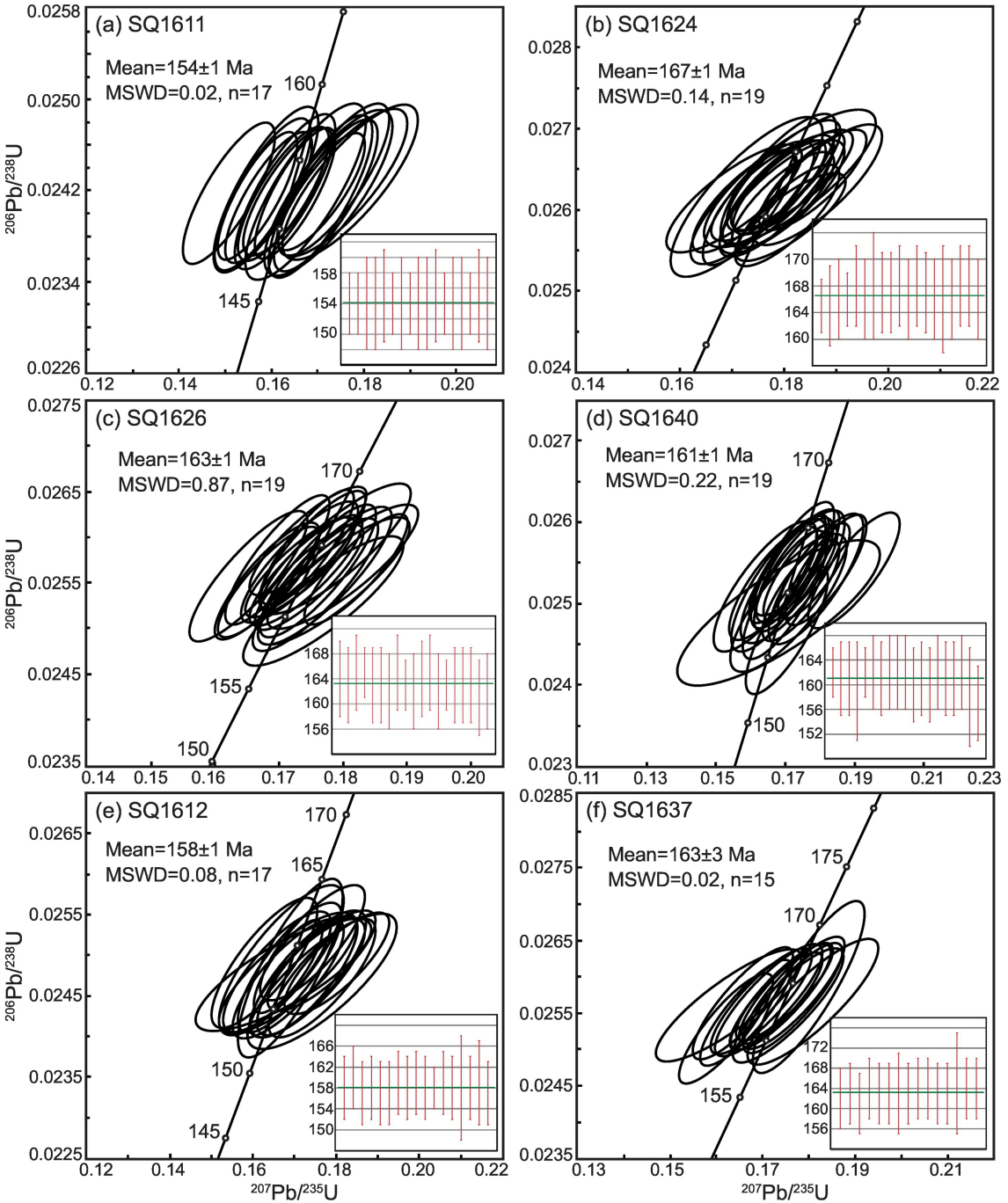
(a) SQ1611
Mean=154±1 Ma
MSWD=0.02, n=17
(b) SQ1624
Mean=167±1 Ma
MSWD=0.14, n=19
(c) SQ1626
Mean=163±1 Ma
MSWD=0.87, n=19
(d) SQ1640
Mean=161±1 Ma
MSWD=0.22, n=19
(e) SQ1612
Mean=158±1 Ma
MSWD=0.08, n=17
(f) SQ1637
Mean=163±3 Ma
MSWD=0.02, n=15
206Pb/238U
207Pb/235U

Figure 7

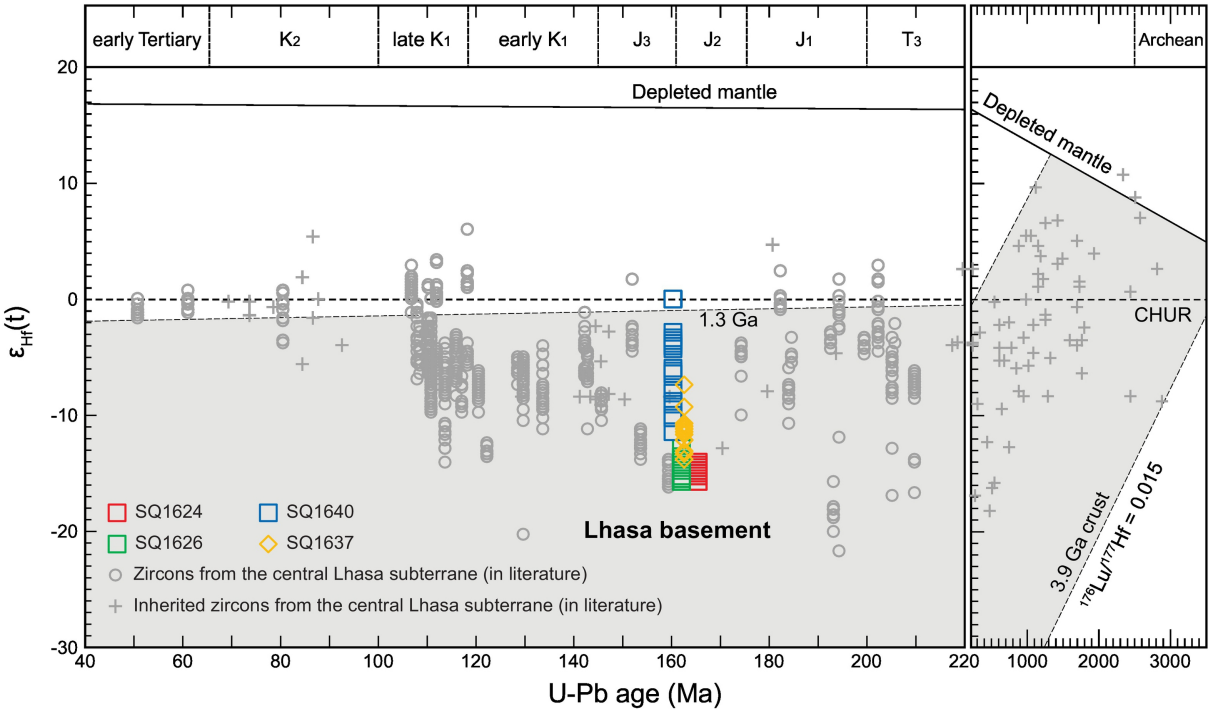
early Tertiary
K2
late K1
early K1
J3
J2
J1
T3
Archean
Depleted mantle
Depleted mantle
CHUR
1.3 Ga
SQ1624
SQ1640
SQ1626
SQ1637
Lhasa basement
Zircons from the central Lhasa subterrane (in literature)
Inherited zircons from the central Lhasa subterrane (in literature)
3.9 Ga crust
176Lu/177Hf = 0.015
εHf(t)
U-Pb age (Ma)

Figure 8

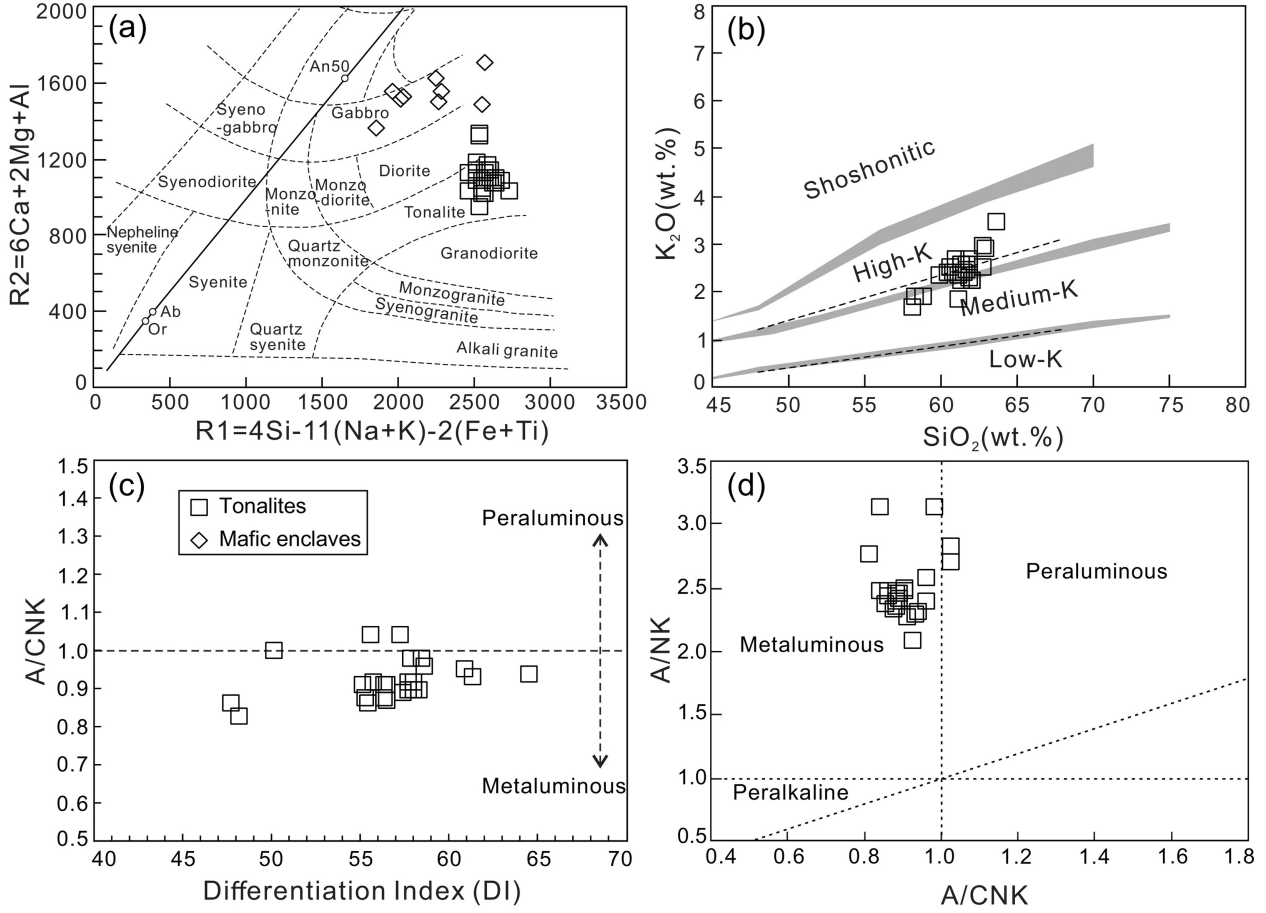
(a)
R2=6Ca+2Mg+Al
R1=4Si-11(Na+K)-2(Fe+Ti)
An50
Syeno-gabbro
Gabbro
Diorite
Syenodiorite
Monzo-nite
Monzo-diorite
Tonalite
Nepheline syenite
Quartz monzonite
Granodiorite
Syenite
Monzogranite
Syenogranite
Ab
Or
Quartz syenite
Alkali granite
(b)
K2O(wt.%)
SiO2(wt.%)
Shoshonitic
High-K
Medium-K
Low-K
(c)
Tonalites
Mafic enclaves
Peraluminous
Metaluminous
A/CNK
Differentiation Index (DI)
(d)
Peraluminous
Metaluminous
Peralkaline
A/NK
A/CNK

Figure 9

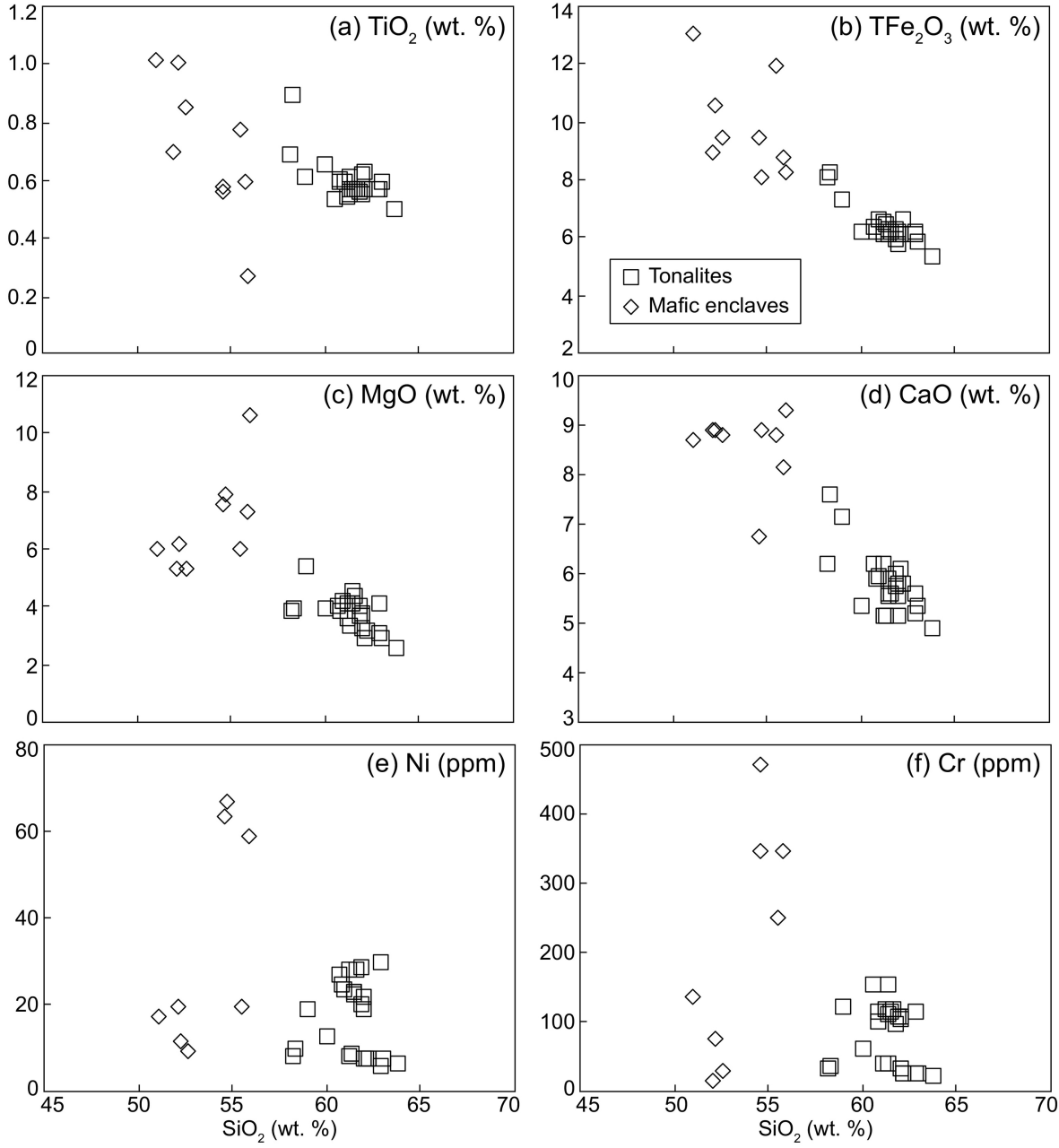
(a) TiO2 (wt. %)
(b) TFe2O3 (wt. %)
Tonalites
Mafic enclaves
(c) MgO (wt. %)
(d) CaO (wt. %)
(e) Ni (ppm)
(f) Cr (ppm)
SiO2 (wt. %)
SiO2 (wt. %)

Figure 10

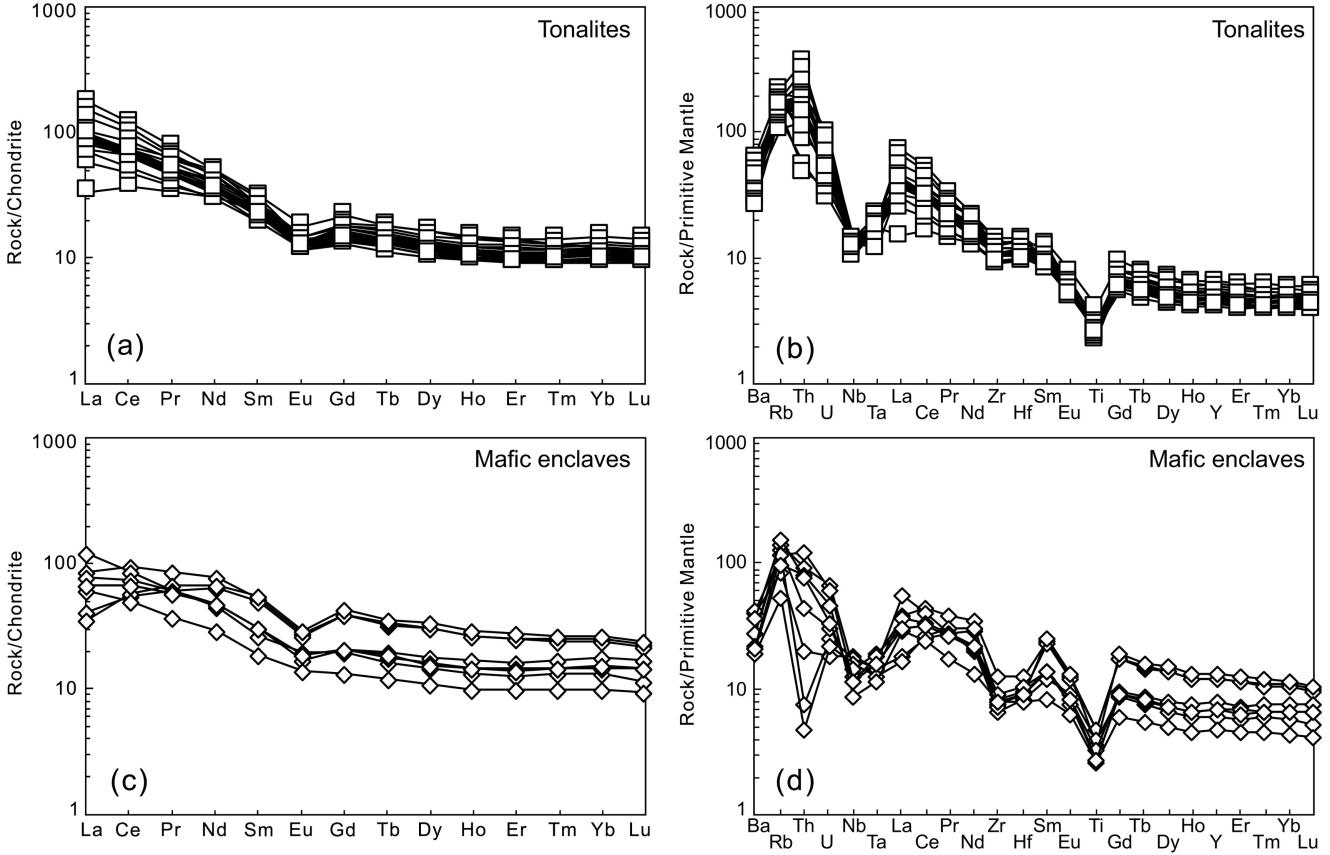
Tonalites
Rock/Chondrite
1000
100
10
1
(a)
La Ce Pr Nd Sm Eu Gd Tb Dy Ho Er Tm Yb Lu
Tonalites
Rock/Primitive Mantle
(b)
Ba Rb Th U Nb Ta La Ce Pr Nd Zr Hf Sm Eu Ti Gd Tb Dy Ho Y Er Tm Yb Lu
Mafic enclaves
(c)
Mafic enclaves
(d)

Figure 11

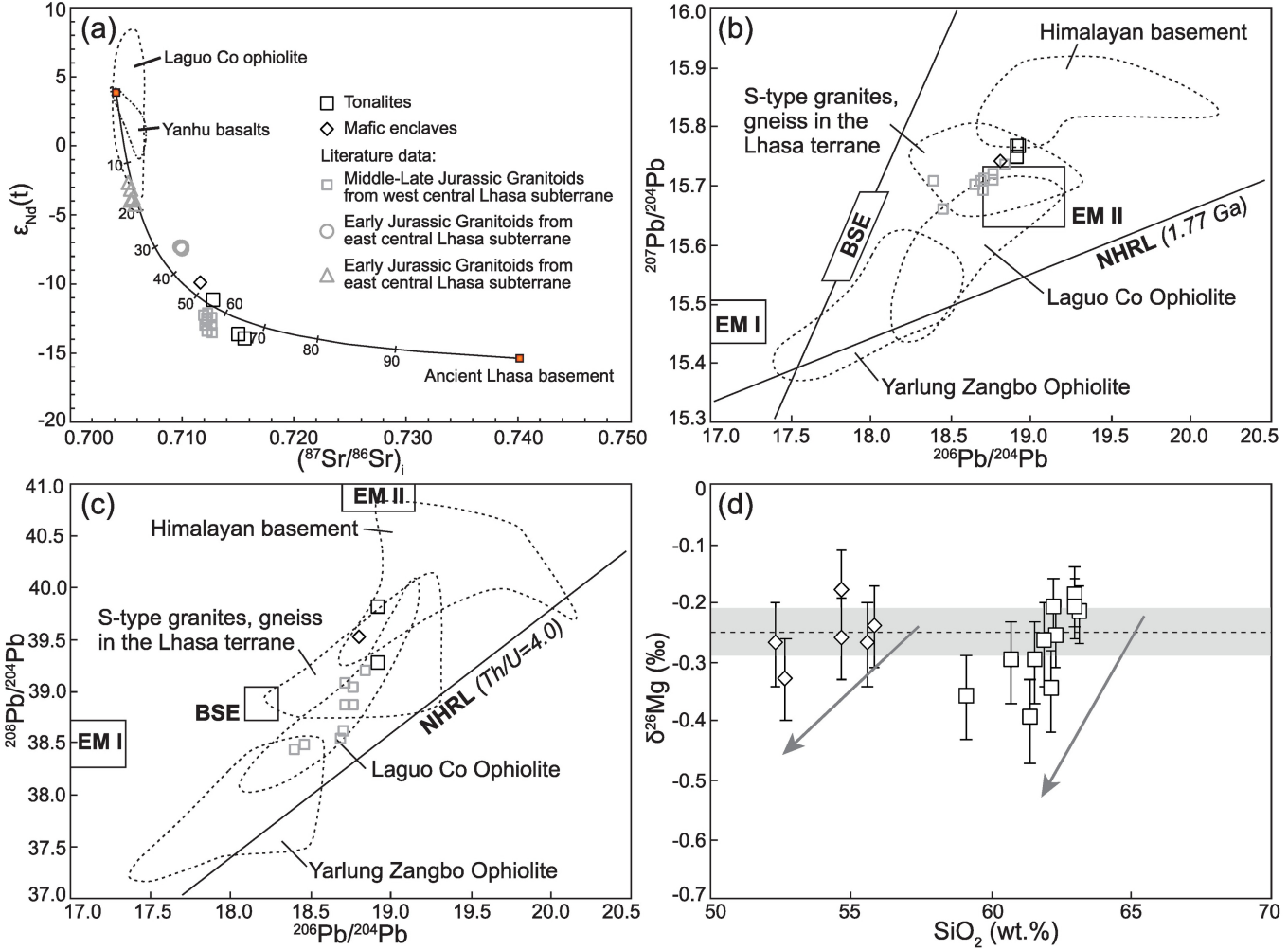
(a)
Laguo Co ophiolite
Yanhu basalts
Tonalites
Mafic enclaves
Literature data:
Middle-Late Jurassic Granitoids from west central Lhasa subterrane
Early Jurassic Granitoids from east central Lhasa subterrane
Early Jurassic Granitoids from east central Lhasa subterrane
Ancient Lhasa basement
εNd(t)
(87Sr/86Sr)i
(b)
Himalayan basement
S-type granites, gneiss in the Lhasa terrane
BSE
EM II
NHRL (1.77 Ga)
Laguo Co Ophiolite
EM I
Yarlung Zangbo Ophiolite
207Pb/204Pb
206Pb/204Pb
(c)
EM II
Himalayan basement
S-type granites, gneiss in the Lhasa terrane
BSE
NHRL (Th/U=4.0)
EM I
Laguo Co Ophiolite
Yarlung Zangbo Ophiolite
208Pb/204Pb
206Pb/204Pb
(d)
δ26Mg (‰)
SiO2 (wt.%)

Figure 12

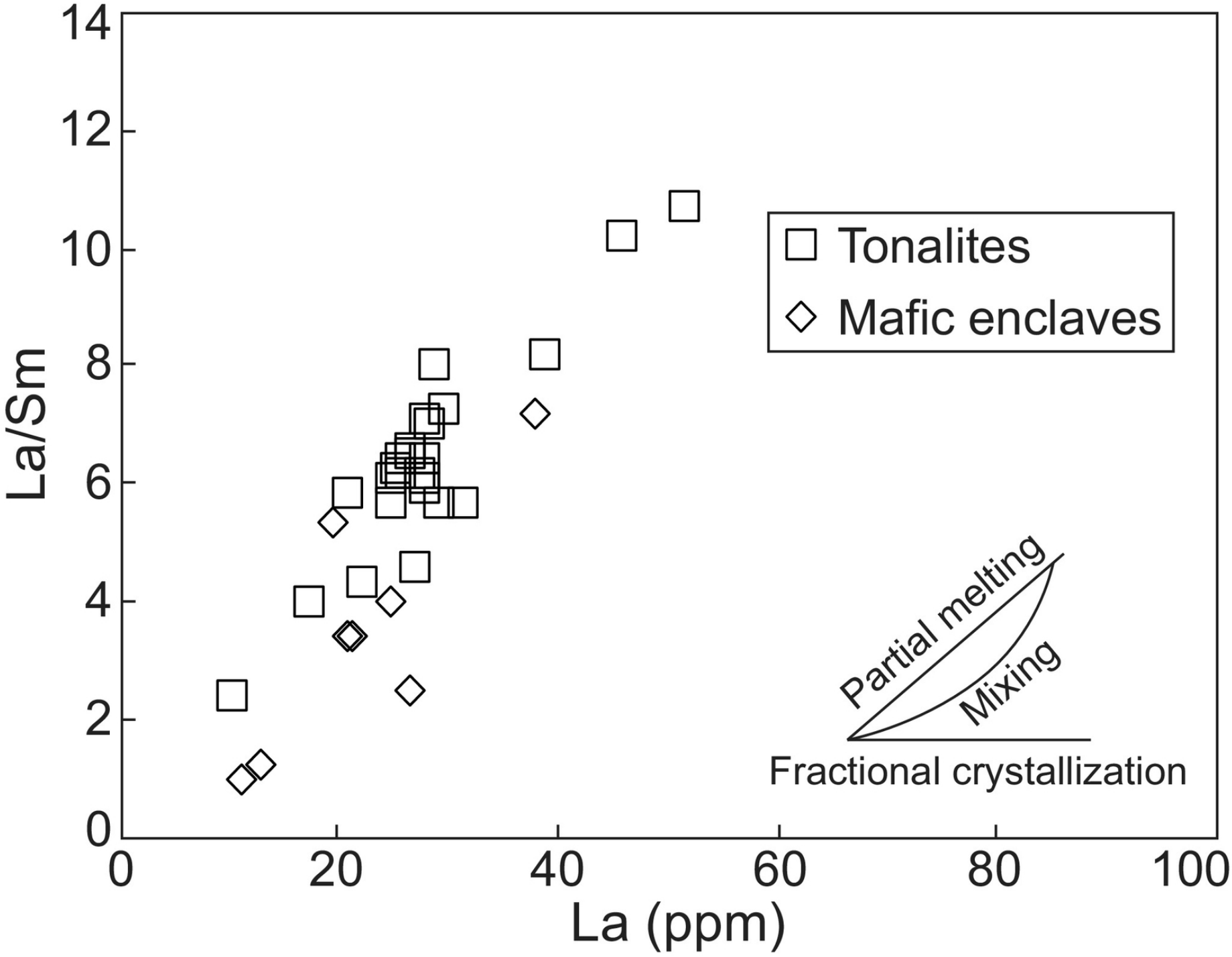
14
12
10
8
6
4
2
0
La/Sm
0
20
40
60
80
100
La (ppm)
Tonalites
Mafic enclaves
Partial melting
Mixing
Fractional crystallization

Figure 13

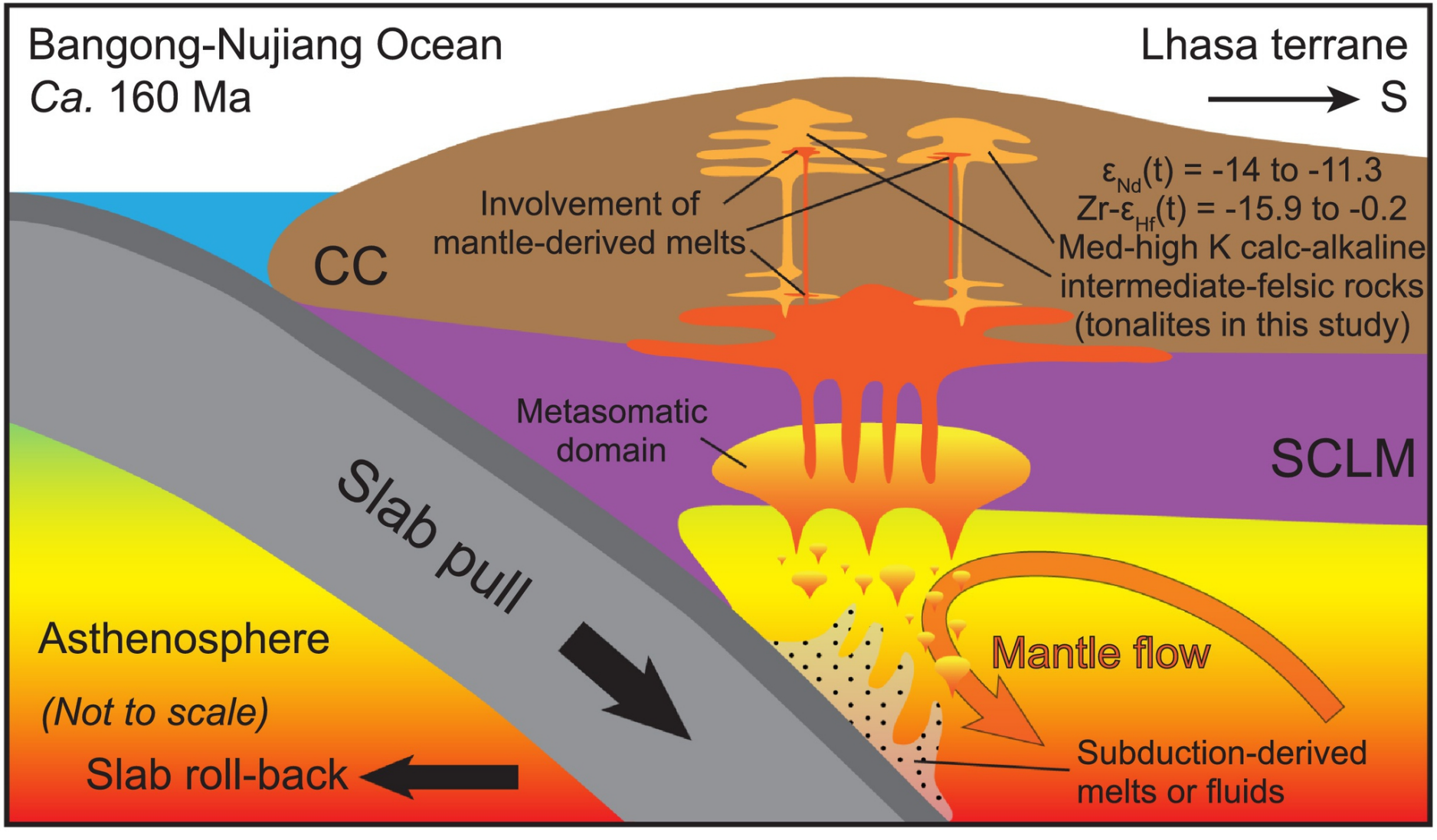
Bangong-Nujiang Ocean
Ca. 160 Ma
Lhasa terrane
S
CC
Involvement of
mantle-derived melts
εNd(t) = -14 to -11.3
Zr-εHf(t) = -15.9 to -0.2
Med-high K calc-alkaline
intermediate-felsic rocks
(tonalites in this study)
Metasomatic
domain
SCLM
Slab pull
Asthenosphere
(Not to scale)
Slab roll-back
Mantle flow
Subduction-derived
melts or fluids

Figure 14